CODED APERTURE IMAGING ON NONPLANAR SURFACES

by

Paul Donald Atcheson

A Thesis Submitted to the Faculty of the

COMMITTEE ON OPTICAL SCIENCES (GRADUATE)

In Partial Fulfillment of the Requirements
For the Degree of

MASTER OF SCIENCE

In the Graduate College

THE UNIVERSITY OF ARIZONA

1 9 7 6

STATEMENT BY AUTHOR

This thesis has been submitted in partial fulfillment of requirements for an advanced degree at The University of Arizona and is deposited in the University Library to be made available to borrowers under rules of the Library.

Brief quotations from this thesis are allowable without special permission, provided that accurate acknowledgment of source is made. Requests for permission for extended quotation from or reproduction of this manuscript in whole or in part may be granted by the head of the major department or the Dean of the Graduate College when in his judgment the proposed use of the material is in the interests of scholarship. In all other instances, however, permission must be obtained from the author.

SIGNED: Paul D. Atchison

APPROVAL BY THESIS DIRECTOR

This thesis has been approved on the date shown below:

Harrison H. Barrett — Dec. 7, 1976

Harrison H. Barrett
Professor of Optical Sciences

Date

ACKNOWLEDGMENTS

As with most human endeavors, this work owes its completion to several people. Discussions with fellow students, especially Robert Simpson and Alan Greynolds, proved invaluable to my understanding of what I was doing. Suggestions related to the experimental work were received from Scott Gordon and Dick Sumner. Discussions with Dr. Roland Shack on aberration theory were very helpful.

Special thanks go to Dr. Harrison Barrett, who, as my research advisor, helped me in all aspects of this work.

Finally, I would like to thank Janet Rowe for typing this thesis so well.

This work was supported in part by Sandia Laboratories, Albuquerque, New Mexico.

TABLE OF CONTENTS

TABLE OF CONTENTS--Continued

LIST OF ILLUSTRATIONS

LIST OF ILLUSTRATIONS--Continued

LIST OF ILLUSTRATIONS--Continued

LIST OF ILLUSTRATIONS--Continued

LIST OF TABLES

ABSTRACT

Fresnel Zone Plate (FZP) imaging of gamma rays can be improved by using an x-ray image intensifier tube, but aberrations are introduced by the nonplanar input screen of the tube. The aberrations are of sufficient size to seriously degrade the final image. In this thesis, the problem of imaging FZP's onto nonplanar surfaces is investigated in a general manner, and two specific types of surfaces, cylindrical and spherical surfaces, are investigated in detail. It is concluded that the predominant image-degrading third-order aberrations in both specific cases are spherical-type aberrations (i.e., aberrations which depend on the fourth power of the pupil radius). Since the spherical-type aberrations are the predominant aberrations, it is proposed to correct for them by distorting the zone plate so that an on-axis point will be imaged as a perfect FZP. It is found that the distorted zone plate will produce larger coma-type aberrations in both the cylindrical surface and the spherical surface imaging systems, but that an improvement is obtained over a small region in the object space.

CHAPTER 1

INTRODUCTION

Coded aperture imaging has been used for several years as a means of increasing collection efficiency without losing resolution in the imaging of high-energy, photon-limited radiation sources. The first type of coding used was a Fresnel zone plate, by Mertz and Young (1961), in the field of x-ray astronomy. Since then, several new types of coding schemes have been used, such as random pinhole arrays (Dicke, 1968), golay patterns (Golay, 1971), and annuli (Walton, 1973), to name a few. The imaging process in all such systems is not truly imaging in the optical sense--the energy of the individual photons is high enough so that there will be, for all practical purposes, no refraction or diffraction at the coded aperture. In other words, the aperture acts as a mask, and the radiation source simply casts a shadow of the aperture onto the imaging surface. The coded image will therefore be a convolution of the source and a scaled version of the aperture. When the image surface is flat and parallel to the aperture, a deconvolution operation will produce a reconstructed image which will look just like the original radiation source. If the image surface is not flat, the reconstructed image will be a degraded version of the original source.

The use of a Fresnel zone plate as the coded aperture is especially easy to understand, because of the physical nature of the

zone plate. A plane wave incident on a zone plate will be focused to a point on the far side of the zone plate; therefore, the zone plate acts as a hologram. This means that a Fresnel zone plate coded aperture imaging system will produce a coded image which can be treated as a hologram.

One field which has seen the use of a Fresnel zone plate as a coded aperture is nuclear medicine. In nuclear medicine, a radionuclide is introduced into the patient's body and collects in the region which is to be observed. Coded aperture imaging is one way to observe the concentration of the radionuclide. One drawback to almost all types of nuclear medicine imaging is a sensitivity/resolution trade-off in most gamma- or x-ray detectors. Film, for example, has a high resolution, but low sensitivity to the radiation of the energies used. Conversely, detectors with high sensitivity generally use thick scintillation crystals and have low resolution. An x-ray image intensifier is one type of detector which is fairly good in both respects--its sensitivity is much better than that of film, and its resolution, though not as high as that of film, is better than that of a detector using a scintillation crystal. As shown in Fig. 1.1, though, the intensifier has a nonplanar input screen, and will produce a distorted coded image if used as the detector in a coded image system. In this thesis, we will examine one possible solution to this problem, namely, replacing the Fresnel zone plate with a distorted zone plate to permit undistorted coded imaging over a small region in the object space.

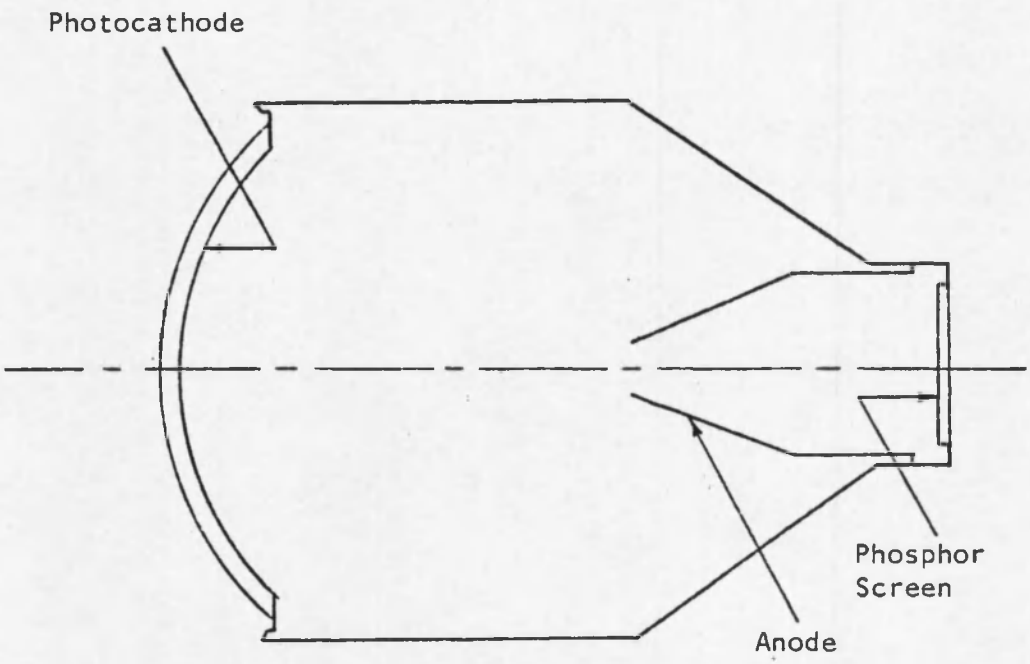

Fig. 1.1. Single Stage Demagnifier Image Intensifier Tube.

CHAPTER 2

THE FRESNEL ZONE PLATE

The Fresnel Zone Plate--a Mathematical Explanation of its Operation

In gamma-ray imaging, a Fresnel zone plate (FZP) is a rotationally-symmetric mask characterized by the transmission function

$$t(r) = \frac{1}{2} + \frac{1}{2}\,\mathrm{sgn}(\sin\alpha r^2). \tag{2.1}$$

It is assumed that no reflection or refraction of gamma rays occurs at the zone plate. In other words, as seen in Fig. 2.1, the FZP acts as a perfect mask to the gamma rays, and the image produced on a plane parallel to the FZP by a gamma-ray point source will be simply an enlarged version of the zone plate, with α in Eq. (2.1) being replaced by

$$\alpha' = \alpha\left[\frac{z_1}{a-R}\right]^2. \tag{2.2}$$

If this coded image is then recorded on film in such a way that the amplitude transmittance of the developed film is proportional to the incident gamma-ray intensity, then the coded image, when illuminated by a plane wave of amplitude A_0, will produce a transmitted wave of amplitude

$$A(r) = A_0\left(\frac{1}{2} + \frac{1}{2}\,\mathrm{sgn}(\sin\alpha' r^2)\right). \tag{2.3}$$

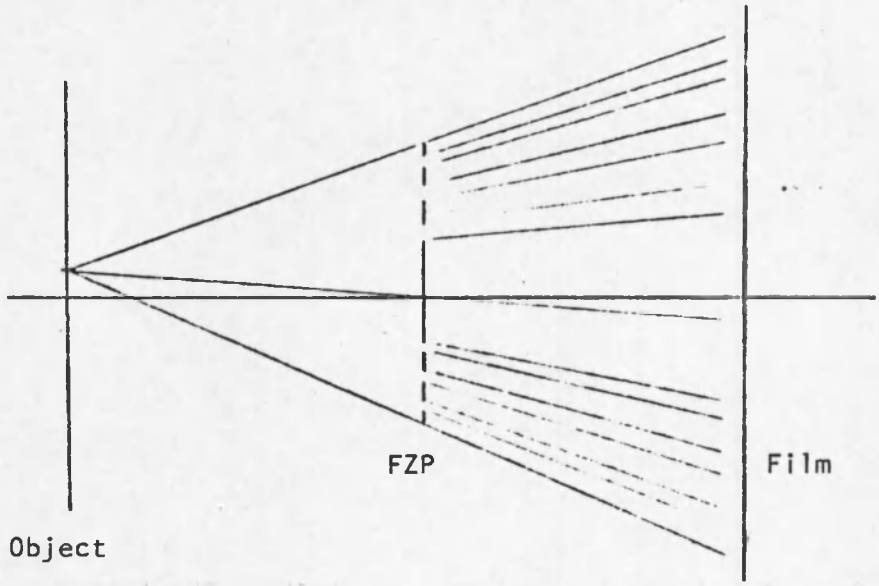

Fig. 2.1. FZP Coded Aperture Imaging Geometry.

Expanding the signum function as a Fourier series gives

$$A(r) = A_0\left(\frac{1}{2} + \frac{1}{2}\sum_{n=-\infty}^{\infty} a_n \exp(i\alpha' r^2 n)\right), \tag{2.4}$$

where a_n is identically zero for all even n and equals $2/\pi n$ for all odd n. This shows that the transmitted wave is comprised of a single undiffracted beam, of amplitude $A_0/2$, and an infinite number of diffracted beams. The amplitude of the diffracted beams is exponentially proportional to r^2; therefore, to a first approximation, they represent converging and diverging spherical waves. Since the first-order approximation of a spherical wave is

$$A'(r) = \exp\left(ikr^2/(2f)\right), \tag{2.5}$$

where

$$k = 2\pi/\lambda, \tag{2.6}$$

and f is the focal length, then the focal lengths of the diffracted beams are given by

$$f_n = \pi/(\lambda\alpha' n). \tag{2.7}$$

Since all of the diffracted orders contain the same object information, we will examine only the n = 1 order, so the coded image amplitude transmittance will be given by

$$A(r) = K \cdot \exp\left(i\alpha' r^2 + i \cdot B(x_1, x_2, x_3, \ldots)\right), \tag{2.8}$$

where $B(x_1, x_2, x_3, \ldots)$ represents the aberrations introduced by the nonplanar-coded image surface.

Properties of the Fresnel Zone Plate

Since the properties of Fresnel zone plates have been described many times in the literature [see, for example, Young (1972), Barrett (1972), Barrett and Horrigan (1973), Henkelman and Bronskill (1974), Barrett and DeMeester (1974), Joy and Houle (1975), and Fonroget, Belvaux, and Lowenthal (1975)], only a short description will be presented here, with no derivation.

The physical appearance of the zone plate is that of a binary mask, comprised of alternately clear and opaque annular zones. The radii of the edges of these zones are equal to

$$r_n = c_1\sqrt{n}, \qquad n = 1,2,3, \ldots, \tag{2.9}$$

where r_n is the radius of the nth zone and c_1 is the radius of the first zone.

The zone plate acts as a lens with an infinite number of focal lengths, given by

$$f_m = c_1^2/\lambda m, \tag{2.10}$$

where λ is the wavelength of the incident radiation. Comparing this to Eq. (2.7), we see that

$$\alpha' = \pi/c_1^2. \tag{2.11}$$

The diffraction-limited spot size is dependent upon the number of zones in the FZP, but with a large enough number of zones, which will be the case here, the diameter of the spot is

$$d = 1.22\lambda f/D, \tag{2.12}$$

where D is the zone plate diameter.

The depth of field is also dependent upon the number of zones, with the expression for a large number of zones being

$$z \approx 3\lambda(f/D)^2, \tag{2.13}$$

where z is the axial displacement which will result in a 50% reduction in the intensity at the center of the point image.

The collection efficiency of gamma rays is proportional to the area of the zone plate, thus a large zone plate can collect many times more quanta of gamma radiation than a pinhole with the same resolution. However, this does not mean that exposure time will necessarily be less in a FZP coded aperture imaging system than in a pinhole imaging system. The reason for this is seen in the signal-to-noise ratio.

Simply stated, FZP imaging obeys quantum noise statistics, with a signal-to-noise ratio (SNR) given by

$$\text{SNR} \propto \sqrt{N}/q, \tag{2.14}$$

where q is the number of point sources in the object field (all of which are assumed to be equal in intensity), and N is the total number of detected quanta. This expression is only valid for small q, since, for large q, the coded image will approach a smooth function. Since the SNR of an equivalent pinhole imaging system is equal to $\sqrt{N/q}$, then it is apparent that, for large objects, a FZP imaging system will have a lower SNR than a pinhole system unless a longer exposure is used for the FZP imaging system. This in turn means that the FZP system will be useful only for imaging systems which are small compared to the field of view, in the case of a continuous object, or for imaging objects which are made up of a small number of bright points.

CHAPTER 3

ABERRATIONS OF SYSTEMS WITH NONPLANAR CODED IMAGE SURFACES

Mathematical Analysis of Systems with Nonplanar Coded Image Surfaces: General Theory

Let a general coded aperture be described by

$$f(x',y') = n, \tag{3.1}$$

and be located an axial distance z_1 to the right of an illuminating gamma-ray source point, as shown in Fig. 3.1. The coded aperture is assumed to be binary and planar, and $f(x',y')$ describes the nth zero-to-one or one-to-zero transition in the transmission of the coded aperture. Let the location of the source point be (x_0,y_0). The spatial distribution of the gamma-ray energy to the right of the coded aperture will then be given by the family of cones defined by the equation

$$f\left[\frac{z_1}{z}\left(x-x_0\left[1-\frac{z}{z_1}\right]\right), \frac{z_1}{z}\left(y-y_0\left[1-\frac{z}{z_1}\right]\right)\right] = n. \tag{3.2}$$

Let the nonplanar coded image surface be described by

$$z = z(x,y). \tag{3.3}$$

Then the x-y projection of the intersection of the family of cones in Eq. (3.2) with the surface in Eq. (3.3) will be given by

$$f\left[\frac{z_1}{z(x,y)}\left(x-x_0\left[1-\frac{z(x,y)}{z_1}\right]\right), \frac{z_1}{z(x,y)}\left(y-y_0\left[1-\frac{z(x,y)}{z_1}\right]\right)\right] = n. \tag{3.4}$$

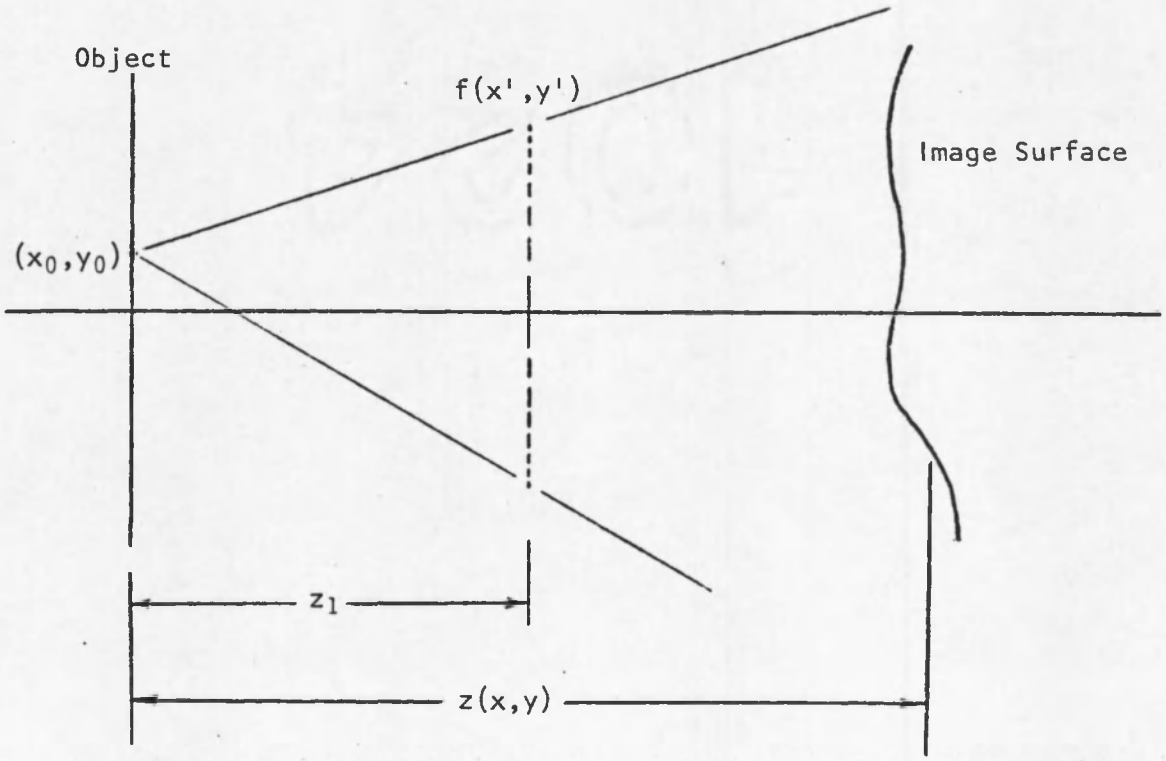

Fig. 3.1. General Coded Aperture Imaging System.

If, in addition, the final coded image is not simply the x-y projection of the image on the nonplanar surface, but can be related to it through the functions

$$x' = g_1(x,y)$$

$$y' = g_2(x,y), \tag{3.5}$$

then it is necessary to invert the functions g_1 and g_2 to find expressions for x and y, and substitute these expressions into Eq. (3.4) before any further analysis can be done.

For a FZP, f(x,y) can be very easily related to fringes in an interferogram. Each fringe on an interferogram represents an optical path difference of one wavelength. On a FZP, each "fringe" is defined by a zero-to-one and a one-to-zero transition; therefore, if we let m be the fringe number on an interferogram, then f(x,y) with a FZP as the coded aperture will represent an interferogram if n = 2m.

As shown in Eq. (2.4), the final expression for a FZP coded image will contain an exponential dependence. This exponential dependence will constitute a phase term which will be added to the phase of any reconstructing wave.

Let the exponential dependence of the final coded image be written as

$$\Phi(x,y) = k \cdot f_1(x,y), \tag{3.6}$$

where k is the wave number of the light which will be used in the reconstruction step, as defined earlier. The phase of the reconstructing wave will be described by

$$\Phi_r(x,y) = k \cdot f_2(x,y), \tag{3.7}$$

so that the image-forming wavefront will have a phase dependence given by

$$\Phi_t(x,y) = k(f_1+f_2). \tag{3.8}$$

To determine the aberrations in this wavefront, it is simply necessary to decompose Eq. (3.8) into a set of aberration expressions which are mathematically complete for the imaging system being used. In the next two sections, examples of this type of calculation will be given, first for a system containing a cylindrical coded image surface, and then for a system containing a spherical coded image surface.

Aberrations Due to Imaging an On-axis FZP onto a Cylindrical Surface

The easiest way to produce a nonplanar surface for coded-aperture imaging is to bend the film which will contain the coded image into a nonplanar shape. For the first part of the experimental work, the nonplanar surface is a cylindrical surface. This section deals with the mathematical analysis of this type of surface.

The physical arrangement is shown in Fig. 3.2. The object point is in plane P_1 and the zone plate is in plane P_2, a distance z_1 from P_1. The cylindrical surface is a section of a right cylinder of radius R, with the axis of rotation parallel to the y-axis and intersecting the z-axis at z = a.

Let the zone plate be described by

$$x^2 + y^2 = c_1{}^2 n. \tag{3.9}$$

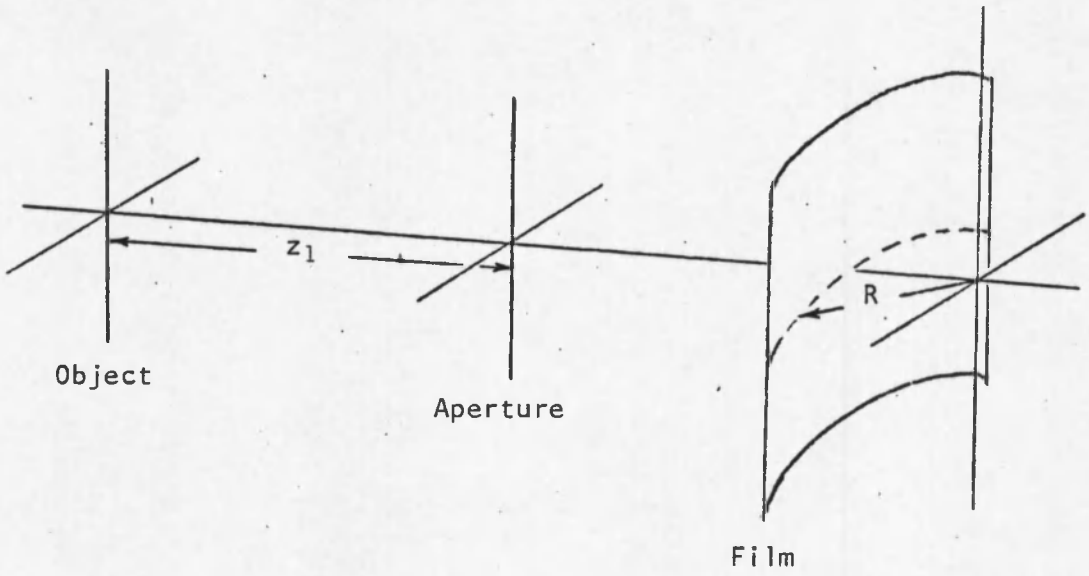

Fig. 3.2. System with Cylindrical Coded Image Surface.

If the illuminating gamma-ray source point is located at (x_0,y_0), then the shadow cast by the zone plate is described by

$$\left[x-x_0\left(1-\frac{z}{z_1}\right)\right]^2+\left[y-y_0\left(1-\frac{z}{z_1}\right)\right]^2 = {c_1}^2 n\,\frac{z^2}{{z_1}^2}\,. \qquad (3.10)$$

The illuminated side of the cylinder is described by

$$z = a-R\sqrt{1-\frac{x^2}{R^2}}\,. \qquad (3.11)$$

Therefore, the x-y projection of the shadow intersecting the cylinder is given by

$$n = \frac{z_1^2}{c_1^2}\left[a-R\sqrt{1-\frac{x^2}{R^2}}\right]^{-2}\left[\left(x-x_0\left[1-\frac{a-R\sqrt{1-\frac{x^2}{R^2}}}{z_1}\right]\right)^2\right.$$

$$\left.+\left(y-y_0\left[1-\frac{a-R\sqrt{1-\frac{x^2}{R^2}}}{z_1}\right]\right)^2\right]. \qquad (3.12)$$

This can be interpreted as the interference pattern of a plane wave propagating in the z-direction and a wave described by a phase expression $\Phi(x,y)$. The interference pattern will exhibit fringe lines at the points

$$(x,y) = 2\pi m, \qquad (3.13)$$

where m is the fringe number. As shown in the previous section, a FZP coded image can be compared to an interferogram by letting n = 2m. Therefore, treating the coded image as an interferogram, we find that the phase of the object wave is given by

$$\Phi(x,y) = \pi\frac{z_1^2}{c_1^2}\left[a-R\sqrt{1-\frac{x^2}{R^2}}\right]^{-2}\left[\left(x-x_0\left[1-\frac{a-R\sqrt{1-\frac{x^2}{R^2}}}{z_1}\right]\right)^2\right.$$

$$\left.+\left(y-y_0\left[1-\frac{a-R\sqrt{1-\frac{x^2}{R^2}}}{z_1}\right]\right)^2\right]. \qquad (3.14)$$

We shall expand this expression in terms of infinite series, making use of the infinite series representations of square roots and

inverse squares:

$$(1-x)^{\frac{1}{2}} = \sum_{n=0}^{\infty} \frac{(-1)^n(\frac{1}{2})!}{n!(\frac{1}{2}-n)!} x^n, \tag{3.15}$$

and

$$(1+x)^{n-2} = \sum_{n=0}^{\infty} (-1)^n(n+1)x^n. \tag{3.16}$$

Rewriting Eq. (3.15) as

$$(1-x)^{\frac{1}{2}} = 1 - x/2 - \sum_{n=2}^{\infty} \frac{(2n-3)!!}{2^n n!} x^n, \tag{3.17}$$

we see that

$$\frac{(\frac{1}{2})!}{n!(\frac{1}{2}-n)!} = \frac{(2n-3)!!}{(2n)!!} \qquad n = 2,3,\cdots . \tag{3.18}$$

We can then rewrite Eq. (3.14) as

$$\begin{aligned}\Phi(x,y) = \frac{\pi z_1^2}{c_1^2(a-R)} \Bigg[& (x_0^2+y_0^2) \frac{a-R}{z_1^2} \\ & + \frac{2}{z_1} (x_0x+y_0y+x_0^2+y_0^2) \sum_{j=0}^{\infty} \frac{R^j}{(a-R)^j} \left(\sum_{k=1}^{\infty} \frac{(2k-3)!!}{(2k)!!} \left[\frac{x}{R}\right]^{2k} \right)^j \\ & + \frac{1}{a-R} \left(x^2+y^2-2(x_0x+y_0y) + x_0^2+y_0^2 \right) \\ & \cdot \sum_{j=0}^{\infty} (-1)^j(j+1) \frac{R^j}{(a-R)^j} \left(\sum_{k=1}^{\infty} \frac{(2k-3)!!}{(2k)!!} \left[\frac{x}{R}\right]^{2k} \right)^j \Bigg].\end{aligned} \tag{3.19}$$

In Eq. (3.19), we see that the first term in the k-series involves (-1)!! in the numerator. Actually, the numerator in this term is simply 1, and the (2k-3)!! representation is only valid for k greater than or equal to 2. However, in an attempt to keep the equations as short as possible, we shall include k = 1 in the infinite series, with the understanding that (-1)!! will always be taken to be equal to 1.

In developing the algebraic descriptions of the "fringe" patterns, we will find it useful to introduce the concept of an illuminating wavelength. Even though the gamma rays emitted by the object have an extremely short wavelength, it is possible to calculate, from the geometry of the imaging system, an equivalent wavelength for the "fringes" in the coded image. In doing this, we make use of the fact that the FZP can represent the interference pattern of a plane wave of wavelength λ_0 and a spherically converging or diverging wave of the same wavelength. The respective zones then represent regions of either constructive or destructive interference. Each zone edge therefore corresponds to a π-phase change over the neighboring zone edges. Looking at the center zone of the FZP, and at the physical parameters of the coded aperture imaging system, we can calculate an equivalent illuminating wavelength using the concept of optical path length. In Fig. 3.3, z_1 is the distance to the zone plate, (a-R) is the axial distance to the image surface, and c_1 is the radius of the first zone of the FZP.

If we let λ_0 be the illuminating wavelength, then

$$AB = AC + \frac{\lambda_0}{2} , \tag{3.20}$$

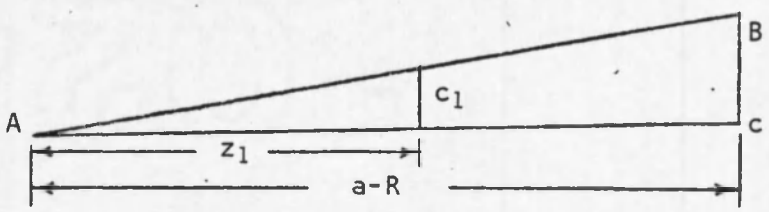

Fig. 3.3. Calculation of an Equivalent Illuminating Wavelength.

or,

$$\lambda_0 = (a-R)\,\frac{c_1^2}{z_1^2}\,, \tag{3.21}$$

where it has been assumed that c_1 is much less than z_1. This expression will always represent a wavelength, but we must remember that it in no way describes the wavelength of any radiation being used at any point in the coding/decoding process. It is simply an artificial wavelength which arises from the recording geometry.

Therefore, if a full-sized transparency of the coded image were to be illuminated by a normal plane wave of wavelength λ_0, then the primary real image would be produced by a wave exactly described by Eq. (3.19).

In this case, though, there are three changes that must be incorporated into Eq. (3.19) before it will describe the image-forming wave in the experimental setup. First of all, the x-y projection is not used. Secondly, the transparency is reduced in size. Thirdly, the final, reduced, coded image is illuminated by a converging beam of wavelength $\lambda \neq \lambda_0$.

In regard to the first change, the film is simply unrolled from the cylindrical form to make the flat coded image, so the change can be accounted for in Eq. (3.19) through a coordinate transformation. Let x' be the circumferential distance corresponding to x. The relation between x and x', as shown in Fig. 3.4, is

$$x' = R\theta. \tag{3.22}$$

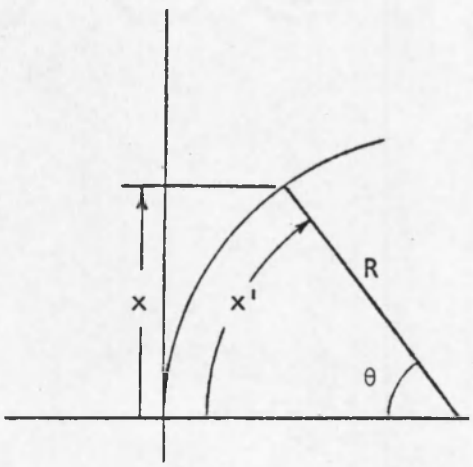

Fig. 3.4. Coordinate Transformation for a Cylindrical Film as the Coded Image Surface.

Therefore,

$$x = R \cdot \sin(x'/R), \tag{3.23}$$

or, when expressed as an infinite series,

$$x = R \sum_{p=0}^{\infty} (-1)^p \frac{1}{(2p+1)!} \left(\frac{x'}{R}\right)^{2p+1}. \tag{3.24}$$

Since x' is the variable of interest in the unrolled coded image, Eq. (3.24) should be substituted into Eq. (3.19), with the result (after letting x' be written as x so that the coded image coordinates will still be x and y)

$$\Phi(x,y) = \frac{2\pi}{\lambda_0} \cdot \frac{1}{2} \left\{ \frac{1}{(a-R)} \left[\left(\sum_{p=0}^{\infty} (-1)^p \frac{1}{(2p+1)!} \frac{x^{2p+1}}{R^{2p}} \right)^2 + y^2 + x_0^2 + y_0^2 \right.\right.$$

$$\left.\left. - 2\left(x_0 \sum_{p=0}^{\infty} (-1)^p \frac{1}{(2p+1)!} \frac{x^{2p+1}}{R^{2p}} + y_0 y \right) \right] \right.$$

$$\cdot \sum_{j=0}^{\infty} (-1)^j (j+1) \frac{R^j}{(a-R)^j} \cdot \left(\sum_{k=1}^{\infty} \frac{(2k-3)!!}{(2k)!!} \right.$$

$$\left. \cdot \left[\sum_{p=0}^{\infty} (-1)^p \frac{1}{(2p+1)!} \frac{x^{2p+1}}{R^{2p+1}} \right]^{2k} \right)^j$$

$$+ \frac{2}{z_1} \left(x_0 \sum_{p=0}^{\infty} (-1)^p \frac{1}{(2p+1)!} \frac{x^{2p+1}}{R^{2p}} + y_0 y + x_0^2 + y_0^2 \right)$$

$$\cdot \sum_{j=0}^{\infty} \frac{R^j}{(a-R)^j} \left(\sum_{k=1}^{\infty} \frac{(2k-3)!!}{(2k)!!} \left[\sum_{p=0}^{\infty} (-1)^p \frac{1}{(2p+1)!} \right.\right.$$

$$\left.\left. \frac{x^{2p+1}}{R^{2p}} \right]^{2k} \right)^j$$

$$\left. + \frac{(a-R)}{z_1^2} (x_0^2 + y_0^2) \right\}. \qquad (3.25)$$

A magnification of the film by a factor of m simply changes all terms involving x and y into terms involving x/m and y/m. The second change mentioned above can therefore be accounted for by letting m be less than one.

In order to account for the spherical converging reconstructing beam, we need to know the phase of the converging beam over a flat plane before we can determine the phase of the beam transmitted by the coded image. The phase of the converging beam is given by the distance from a point on the wavefront to the focus, therefore, from Fig. 3.5, we see that

$$\Phi_r(r) = \frac{2\pi}{\lambda} z_r \sqrt{1 + \frac{r^2}{z_r^2}} \, . \tag{3.26}$$

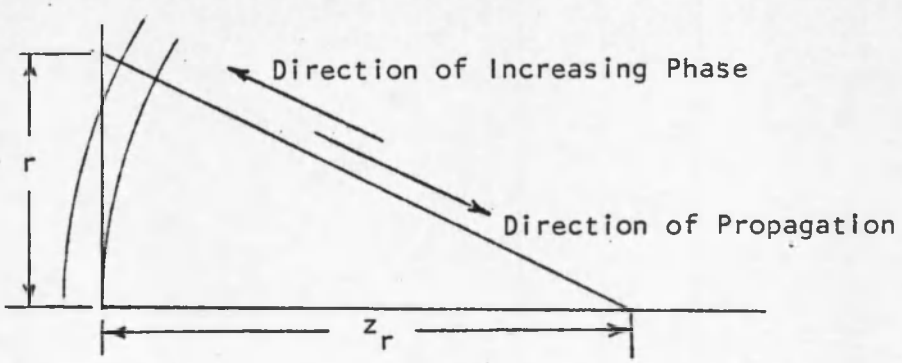

Fig. 3.5. Phase of a Spherically Converging Beam.

Using Eq. (3.15), we can rewrite this as

$$\Phi_r(r) = \frac{2\pi}{\lambda} \sum_{i=0}^{\infty} \frac{(\frac{1}{2})!\, z_r}{i!(\frac{1}{2}-i)!} \cdot \left(\frac{r}{z_r}\right)^{2i}, \tag{3.27}$$

where z_r is the distance from the coded image to the focus of the converging beam.

The phase of the first diffracted order to the right of the coded image is then

$$\Phi_d(x,y) = \Phi(x/m, y/m) + \Phi_r(r), \tag{3.28}$$

where

$$r = (x^2 + y^2)^{\frac{1}{2}}. \tag{3.29}$$

If we define $\mu = \lambda/\lambda_0$, then the final wavefront description can be written for the wave forming the reconstructed image:

$$\Phi_d(x,y) = \frac{2\pi}{\lambda} \sum_{i=0}^{\infty} \frac{(\frac{1}{2})!}{i!(\frac{1}{2}-i)!} \frac{(x^2+y^2)^i}{z_r^{2i-1}} + \frac{2\pi}{\lambda} \cdot \frac{\mu}{2} \left\{ \frac{1}{a-R} \left[\frac{x^2+y^2}{m^2} \right.\right.$$

$$- \frac{2}{m}(x_0 x + y_0 y) + x_0^2 + y_0^2 + 2\left(\frac{x}{m} - x_0\right) \sum_{p=1}^{\infty} \frac{(-1)^p}{(2p+1)!} \frac{x^{2p+1}}{R^{2p} m^{2p+1}}$$

$$\left. + \left(\sum_{p=1}^{\infty} \frac{(-1)^p}{(2p+1)!} \frac{x^{2p+1}}{R^{2p} m^{2p+1}} \right)^2 \right] \sum_{j=0}^{\infty} (-i)^j (j+1) \frac{R^j}{(a-R)^j} \left(\sum_{k=1}^{\infty} \frac{(2k-3)!!}{(2k)!!} \right.$$

$$\left. \left. \cdot \frac{1}{R^{2k}} \left[\frac{x^2}{m^2} + 2\frac{x}{m} \sum_{p=1}^{\infty} \frac{(-1)^p}{(2p+1)!} \frac{x^{2p+1}}{R^{2p} m^{2p+1}} + \left(\sum_{p=1}^{\infty} \frac{(-1)^p}{(2p+1)!} \cdot \frac{x^{2p+1}}{R^{2p} m^{2p+1}} \right)^2 \right]^k \right)^j \right\}$$

$$+\frac{2}{z_1}\left[\frac{x_0x+y_0y}{m}+{x_0}^2+{y_0}^2+x_0\sum_{p=1}^{\infty}\frac{(-1)^p}{(2p+1)!}\frac{x^{2p+1}}{R^{2p}m^{2p+1}}\right]\cdot\sum_{j=0}^{\infty}\frac{R^j}{(a-R)^j}$$

$$\cdot\left(\sum_{k=1}^{\infty}\frac{(2k-3)!!}{(2k)!!}\quad\frac{1}{R^{2k}}\left[\frac{x^2}{m^2}+2\,\frac{x}{m}\sum_{p=1}^{\infty}\frac{(-1)^p}{(2p+1)!}\frac{x^{2p+1}}{R^{2p}m^{2p+1}}\right.\right.$$

$$\left.\left.+\left(\sum_{p=1}^{\infty}\frac{(-1)^p}{(2p+1)!}\cdot\frac{x^{2p+1}}{R^{2p}m^{2p+1}}\right)^2\right]^k\right)^j+\frac{a-R}{{z_1}^2}({x_0}^2+{y_0}^2)\Bigg\}. \qquad (3.30)$$

Equation (3.30) may look like a rather cumbersome equation, but it must be remembered that it totally describes the wavefront. If only the description through third-order aberrations is required, then the expression becomes greatly simplified, if not shorter, in that the infinite series disappears.

A small problem arises in the calculation of aberrations for a system using a coded image made on a cylindrical film. The coded image does not exhibit rotational symmetry, but instead has two mutually-orthogonal planes of symmetry. One plane of symmetry is the x-z plane, and the other is the y-z plane. Obviously, if a coded image is made using a source at (x_0,y_0) with this film surface and a rotationally-symmetric coded aperture, then the coded image will be identical, except for rotation, to coded images made using sources located at $(x_0,-y_0)$, $(-x_0,y_0)$, and $(-x_0,-y_0)$. In a rotationally-symmetric system, any rotation of the source will result in an identical coded image.

The consequence of the change in symmetry is that the aberrations used for describing rotationally-symmetric systems will not completely describe the system that uses a coded image made on a cylindrical film surface. For this reason, we will expand the wavefront in terms of the following parameters (see Fig. 3.6): ρ^2, σ^2, $\rho\sigma \cos(\gamma+\phi)$, $\rho\sigma \cos(\gamma-\phi)$, $\rho^2 \cos 2\phi$, $\sigma^2 \cos 2\gamma$.

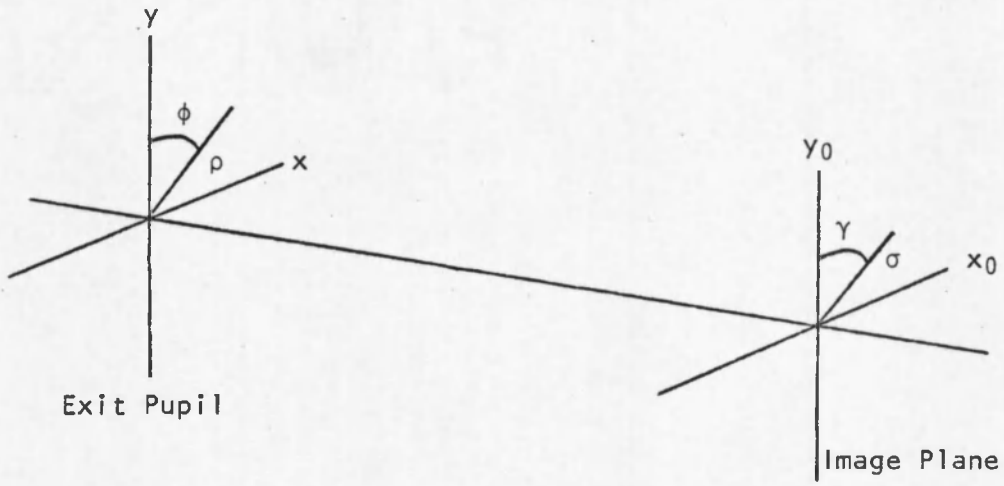

Fig. 3.6. Image Space Parameters of a System with Two Mutually-orthogonal Symmetry Axes.

A more complete discussion of this means of describing the aberrations, and an expression for determining the dependence of the rms spot size on the third-order aberrations, is given in Appendix A.

As can be seen in Fig. 3.6,

$$x^2 + y^2 = \rho^2$$

$$x_0^2 + y_0^2 = \sigma^2$$

$$x^2 = \tfrac{1}{2}(\rho^2 - \rho^2 \cos 2\phi)$$

$$x_0^2 = \tfrac{1}{2}(\sigma^2 - \sigma^2 \cos 2\gamma)$$

$$x_0 x = \tfrac{1}{2}\left(\rho\sigma \cos(\gamma-\phi) - \rho\sigma \cos(\gamma+\phi)\right)$$

$$x_0 x + y_0 y = \rho\sigma \cos(\gamma-\phi), \qquad (3.31)$$

and Eq. (3.30) becomes

$$\Phi_d(\rho,\sigma,\phi,\gamma) = \frac{2\pi}{\lambda} \cdot \left\{ \sum_{i=0}^{\infty} \frac{(\frac{1}{2})!}{i!(\frac{1}{2}-1)!} \cdot \frac{\rho^{2i}}{z_r^{2i-1}} + \frac{\mu}{m^2(a-R)} \left[\frac{\rho^2}{m^2} - 2\frac{\rho\sigma \cos(\gamma-\phi)}{m} \right.\right.$$

$$+ \sigma^2 + 2 \sum_{p=1}^{\infty} \frac{(-1)^p}{(2p+1)!} \cdot \frac{(\rho^2-\rho^2 \cos 2\phi)^{p+1}}{2^{p+1} m^{2p+2} R^{2p}} - \left(\rho\sigma \cos(\gamma-\phi) \right.$$

$$\left.\left. - \rho\sigma \cos(\gamma+\phi)\right) \sum_{p=1}^{\infty} \frac{(-1)^p}{(2p+1)!} \frac{(\rho^2-\rho^2 \cos 2\phi)^p}{2^p m^{2p+1} R^{2p}} + \frac{\rho^2 - \rho^2 \cos 2\phi}{2} \right.$$

$$\left. \cdot \left(\sum_{p=1}^{\infty} \frac{(-1)^p}{(2p+1)!} \frac{(\rho^2-\rho^2 \cos 2\phi)^p}{2^p m^{2p+1} R^{2p}} \right)^2 \right] \sum_{j=0}^{\infty} (-1)^j (j+1) \frac{R^j}{(a-R)^j}$$

$$\cdot \left(\sum_{k=1}^{\infty} \frac{(2k-3)!!}{(2k)!!} \frac{1}{R^{2k}} \left[\frac{\rho^2-\rho^2 \cos 2\phi}{2m^2} + 2 \sum_{p=1}^{\infty} \frac{(-1)^p}{(2p+1)!} \frac{(\rho^2-\rho^2 \cos 2\phi)^{p+1}}{2^{p+1} m^{2p+2} R^{2p}} \right.\right.$$

$$\left.\left. + \frac{\rho^2-\rho^2 \cos 2\phi}{2} \left(\sum_{p=1}^{\infty} \frac{(-1)^p}{(2p+1)!} \frac{(\rho^2-\rho^2 \cos 2\phi)^p}{2^p m^{2p+1} R^{2p}} \right)^2 \right]^k \right)^j$$

$$+ \frac{\mu}{z_1}\left[\frac{\rho\sigma\cos(\gamma-\phi)}{m} + \sigma^2 + \frac{\rho\sigma\cos(\gamma-\phi) - \rho\sigma\cos(\gamma+\phi)}{2}\right.$$

$$\cdot \sum_{p=1}^{\infty} \frac{(-1)^p}{(2p+1)!} \frac{(\rho^2-\rho^2\cos 2\phi)^p}{2^p m^{2p+1} R^{2p}}\Bigg] \sum_{j=0}^{\infty} \frac{R^j}{(a-R)^j}\left(\sum_{k=1}^{\infty} \frac{(2k-3)!!}{(2k)!!} \quad \frac{1}{R^{2k}}\right.$$

$$\cdot \left[\frac{\rho^2-\rho^2\cos 2\phi}{2m^2}\left(1 + \sum_{p=1}^{\infty} \frac{(-1)^p}{(2p+1)!} \frac{(\rho^2-\rho^2\cos 2\phi)^p}{2^p m^{2p} R^{2p}}\right)^2\right]^k\Bigg)^j$$

$$\left. + \frac{\mu(a-R)}{2z_1^2}\sigma^2\right\}. \tag{3.32}$$

Again, this is the complete description of the wavefront. If the terms through third-order are the only ones of interest, then the wavefront is described by

$$\Phi_d(\rho,\sigma,\phi,\gamma) = \Phi^0 + \Phi^1 + \Phi^2 + \Phi^3, \tag{3.33}$$

where

$$\Phi^0 = \frac{2\pi}{\lambda} z_r , \tag{3.34}$$

$$\Phi^1 = \frac{2\pi}{\lambda}\left\{\rho^2\left[\frac{1}{2z_r} + \frac{\mu}{2m^2(a-R)}\right] - \rho\sigma\cos(\gamma-\phi)\left[\frac{\mu}{m(a-R)} - \frac{\mu}{mz_1}\right]\right.$$

$$\left. + \sigma^2\left[\frac{\mu}{2(a-R)} + \frac{\mu}{z_1} + \frac{\mu(a-R)}{2z_1^2}\right]\right\}, \tag{3.35}$$

$$\Phi^2 = 0, \tag{3.36}$$

$$\Phi^3 = \frac{2\pi}{\lambda}\left\{\rho^4\left[-\frac{1}{8z_r^3} - \frac{\mu}{4m^4R(a-R)^2} - \frac{\mu}{24m^4R^2(a-R)}\right]\right.$$

$$+ \rho^4\cos 2\phi\left[\frac{\mu}{24m^4R^2(a-R)} + \frac{\mu}{4m^4R(a-R)^2}\right]$$

$$+ \rho^4\cos^2 2\phi\left[-\frac{\mu}{24m^4R^2(a-R)}\right]$$

$$+ \rho^3\sigma\cos(\gamma-\phi)\left[-\frac{\mu}{2m^3R(a-R)^2} + \frac{\mu}{24m^3R^2(a-R)} + \frac{\mu}{4m^3z_1R(a-R)} - \frac{\mu}{24m^3z_1R^2}\right]$$

$$+ \rho^3\sigma\cos(\gamma-\phi)\cos 2\phi\left[-\frac{\mu}{4m^3R^2(a-R)} + \frac{\mu}{24m^3R^2z_1} + \frac{\mu}{2m^3R(a-R)^2} - \frac{\mu}{4m^3z_1R(a-R)}\right]$$

$$+ \rho^3\sigma\cos(\gamma+\phi)\left[-\frac{\mu}{4m^3R^2(a-R)} + \frac{\mu}{24m^3z_1R^2}\right]$$

$$+ \rho^3\sigma\cos(\gamma+\phi)\cos 2\phi\left[\frac{\mu}{4m^3R^2(a-R)} - \frac{\mu}{24m^3z_1R^2}\right]$$

$$+ \rho^2\sigma^2\left[-\frac{\mu}{4m^2R(a-R)^2} + \frac{\mu}{4m^2z_1R(a-R)}\right]$$

$$\left.+ \rho^2\sigma^2\cos 2\phi\left[\frac{\mu}{4m^2R(a-R)^2} - \frac{\mu}{4m^2z_1R(a-R)}\right]\right\}. \tag{3.37}$$

Equation (3.34) represents simply a constant phase which is added to all wavefronts and will be ignored from this point onward. Equation (3.35) gives the Guassian imaging characteristics.

Equations (3.36) and (3.37) give, respectively, the second- and third-order aberrations. First, we will look at the Gaussian characteristics.

The Gaussian image plane is located a distance z_g from the coded image, given by

$$\Phi^1 = \frac{2\pi}{\lambda} \cdot \frac{\rho^2}{2z_g} . \tag{3.38}$$

For this system, then,

$$z_g = \frac{z_r}{1 + \frac{\mu z_r}{m^2(a-R)}} . \tag{3.39}$$

Also, the coordinates of the Gaussian image point (a_g,b_g) are given by the x and y coefficients in Φ^1,

$$\Phi^1 = \frac{2\pi}{\lambda} \cdot \frac{1}{2z_g} (x^2 + y^2 - 2a_g x - 2b_g y). \tag{3.40}$$

Since $x_0 x + y_0 y = \rho\sigma \cos(\gamma-\phi)$, then

$$a_g = -x_0 \frac{\mu z_g z_2}{m z_1 (a-R)} , \tag{3.41}$$

and

$$b_g = -y_0 \frac{\mu z_g z_2}{m z_1 (a-R)} , \tag{3.42}$$

where $z_2 = (a-R) - z_1$.

If we define a system magnification to be m_s, where $a_g = x_0 m_s$, then

$$m_s = -m \frac{\mu z_2 z_r}{z_1\left(\mu z_r + m^2(a-R)\right)} . \tag{3.43}$$

To find the third-order aberrations, we must compare the phase of the actual wavefront to that of a reference wavefront centered on the Gaussian image point. The third-order term of the Gaussian reference sphere is

$$\Phi_g{}^3 = \frac{2\pi}{\lambda}\left(-\frac{1}{8z_g{}^3}\right)\Big[\rho^4 - 4\rho^3\sigma\cos(\gamma-\phi) + 2\rho^2\sigma^2 + 4\rho^2\sigma^2\cos^2(\gamma-\phi) - 4\rho\sigma^3\cos(\gamma-\phi) + \sigma^4\Big]. \tag{3.44}$$

The third-order aberrations of the reconstructing wavefront are therefore given by the difference between Eqs. (3.37) and (3.44), or

$$W^3 = \frac{\lambda}{2\pi}\left[\Phi^3 - \Phi_g{}^3\right]. \tag{3.45}$$

One change must be made in the expressions for Φ^3 before it can be used in Eq. (3.45). The x_0 and y_0 values in Eq. (3.37) refer to the coordinates in object space, whereas the σ values in Eq. (3.44) refer to the coordinates in image space; therefore, the field parameter in Eq. (3.37) must be multiplied by the system magnification.

As shown in Appendix A, the total aberration function is defined by

$$W = \sum^{(6)} W_{abcdef}\rho'^a\sigma^b\left(\cos(\gamma-\phi)\right)^c\left(\cos(\gamma+\phi)\right)^d(\cos 2\phi)^e(\cos 2\gamma)^f. \tag{3.46}$$

Using this representation, and solving Eq. (3.45), we find that the wavefront is described by the following aberration coefficients:

$$W_{400000} = -\frac{\mu}{m^2(a-R)}\left[\frac{6R+(a-R)}{24m^2R^2(a-R)} - \frac{3}{8z_r^2} - \frac{3\mu}{8m^2z_r(a-R)} - \frac{\mu^2}{8m^4(a-R)^2}\right]\rho_{max}^4, \tag{3.47}$$

$$W_{400010} = \frac{\mu}{m^2(a-R)}\left[\frac{6R+(a-R)}{24m^2R^2(a-R)}\right]\rho_{max}^4, \tag{3.48}$$

$$W_{400020} = -\frac{\mu}{m^2(a-R)}\left[\frac{1}{24m^2R^2}\right]\rho_{max}^4, \tag{3.49}$$

$$W_{311000} = -\frac{\mu}{m^2(a-R)}\left[\frac{12z_1R-(a-R)(6R-z_2)}{24mz_1R^2(a-R)} + \frac{m^2(a-R)}{2\mu z_r^3} + \frac{3}{2z_r^2} + \frac{3\mu}{2m^2z_r(a-R)} + \frac{\mu^2}{2m^4(a-R)^2}\right]\rho_{max}^3, \tag{3.50}$$

$$W_{311010} = \frac{\mu}{m^2(a-R)}\left[\frac{12z_1R-(a-R)(6R-z_2)}{24mz_1R^2(a-R)}\right]\rho_{max}^3, \tag{3.51}$$

$$W_{310100} = \frac{\mu}{m^2(a-R)}\left[\frac{6z_1-(a-R)}{24mR^2z_1}\right]\rho_{max}^3, \tag{3.52}$$

$$W_{310110} = -W_{310100}, \tag{3.53}$$

$$W_{220000} = \frac{\mu}{m^2(a-R)}\left[\frac{z_2}{4Rz_1(a-R)} + \frac{m^2(a-R)}{4\mu z_r^3} + \frac{3}{4z_r^2} + \frac{3\mu}{4m^2z_r(a-R)} + \frac{\mu^2}{4m^4(a-R)^2}\right]\rho_{max}^2, \tag{3.54}$$

$$W_{220010} = -\frac{\mu}{m^2(a-R)}\left[\frac{z_2}{4Rz_1(a-R)}\right]\rho_{max}^2, \tag{3.55}$$

$$W_{222000} = \frac{\mu}{m^2(a-R)}\left[\frac{m^2(a-R)}{2\mu z_r^3} + \frac{3}{2z_r^2} + \frac{3\mu}{2m^2 z_r(a-R)} + \frac{\mu^2}{2m^4(a-R)^2}\right]\rho_{max}^2, \tag{3.56}$$

$$W_{131000} = W_{222000}/\rho_{max}, \tag{3.57}$$

$$W_{040000} = W_{222000}/4\rho_{max}^2. \tag{3.58}$$

In these expressions, ρ_{max} refers to the maximum radius in the exit pupil, and appears because the ρ in Eq. (3.46) is a normalized parameter,

$$\rho' = (x^2 + y^2)^{\frac{1}{2}}/\rho_{max}. \tag{3.59}$$

If r_c' is the maximum zone plate radius, then

$$\rho_{max} = mr_c'\left(\frac{a-R}{z_1}\right). \tag{3.60}$$

To get an idea of how badly aberrated a wavefront is, we can look at several criteria, such as rms wavefront error, rms spot size, and the maximum intensity of the point image. In this paper, we will use a comparison of the rms spot size and the diffraction-limited spot size as an indication of the image quality of the image, mainly because that will be somewhat easier to calculate than the other criteria.

For a FZP, the diffraction-limited spot size is given by [see Stigliani, Mittra, and Semonin (1967)]

$$d = \beta\lambda f/D, \tag{3.61}$$

where f/D is the f/# of the particular zone plate order, and β is a numerical factor which is dependent upon the number of zones. For a sufficiently large number of zones, β can be set equal to 1.22. In terms of the parameters used above,

$$f/D = \frac{z_g}{2\rho_{max}}, \tag{3.62}$$

and

$$\lambda = \mu(a-R)\frac{c_1^2}{z_1^2}. \tag{3.63}$$

Therefore,

$$d = 0.61\ \mu z_g(a-R)\frac{c_1^2}{\rho_{max} z_1^2}. \tag{3.64}$$

If the aberration-limited spot size is given by

$$\bar{\varepsilon} = \frac{z_g}{\rho_{max}} W(\sigma,\gamma), \tag{3.65}$$

where $W(\sigma,\gamma)$ contains all of the aberration dependence of the spot size, then the ratio of the aberration-limited spot size to the diffraction-limited spot size is given by

$$\frac{\bar{\varepsilon}}{d} = \frac{z_1^2}{0.61\ \mu(a-R)c_1^2} W(\sigma,\gamma), \tag{3.66}$$

or

$$\frac{\bar{\varepsilon}}{d} = \frac{1}{0.61\lambda} W(\sigma,\gamma). \tag{3.67}$$

In other words, if $W(\sigma,\gamma)$ is less than roughly $3.6\ 10^{-5}$ cm, or $(0.61\lambda)^{-1}$, then there can be only a small improvement in the final image by correcting the aberrations and may not be worth the trouble.

In Chapter 5, we will investigate the use of the rms spot size criterion as a measure of image quality, in addition to presenting examples of the type of imagery which can be expected in using a cylindrical surface as a coded-image surface.

Aberrations Due to Imaging an On-axis FZP onto a Spherical Surface

The impetus for the calculations being performed in this paper is the desire to use an x-ray image intensifier tube in a conventional gamma-ray FZP coded-aperture imaging system. The main problem encountered in doing this is the distortion present in the coded image due to the nonplanar input screen in the intensifier. As a first approximation, the screen can be described as a section of a sphere. Therefore, an analysis of imaging a coded aperture onto a spherical surface will approximately describe the aberrations that will be introduced by the intensifier tube.

The physical arrangement is similar to that of the system with the cylindrical coded-image surface, with a spherical surface centered at z = a being used instead of a cylindrical surface.

As before, the FZP is described by

$$x^2 + y^2 = c_1{}^2 n, \tag{3.68}$$

and the shadow cast is again described by

$$\left[x-x_0\left(1-\frac{z}{z_1}\right)\right]^2+\left[y-y_0\left(1-\frac{z}{z_1}\right)\right]^2 = {c_1}^2 n\,\frac{z^2}{{z_1}^2}\,. \tag{3.69}$$

In this case, though, the illuminating surface is described by

$$z = a-R\sqrt{1-\frac{x^2+y^2}{R^2}}\,. \tag{3.70}$$

If we follow the same procedure as before, an equation very similar to Eq. (3.19) can be derived:

$$\Phi(x,y) = \frac{2\pi}{\lambda_0}\;\frac{1}{2}\left\{\frac{x^2+y^2-2(x_0x+y_0y)+{x_0}^2+{y_0}^2}{a-R}\left[\sum_{j=0}^{\infty}(-i)^j(j+1)\,\frac{R^j}{(a-R)^j}\right.\right.$$

$$\left.\cdot\left(\sum_{k=1}^{\infty}\frac{(2k-3)!!}{(2k)!!}\left[\frac{x^2+y^2}{R2}\right]^k\right)^j\right]+\frac{2}{z_1}\,(x_0x+y_0y+{x_0}^2+{y_0}^2)$$

$$\left.\cdot\;\sum_{j=0}^{\infty}\frac{R^j}{(a-R)^j}\left(\sum_{k=1}^{\infty}\frac{(2k-3)!!}{(2k)!!}\left[\frac{x^2+y^2}{R2}\right]^k\right)^j+\frac{a-R}{{z_1}^2}\,({x_0}^2+{y_0}^2)\right\}. \tag{3.71}$$

In this case, the coded image cannot be simply unrolled from the spherical surface (cartographers have attacked the problem of mapping a spherical surface onto a flat plane without introducing distortion for centuries, with little success), so, for the purposes of this thesis, we will assume that the final coded image will be the x-y projection of the image on the surface. Again, the reconstruction will

involve a size-reduction and illumination with a spherically converging beam. Since the system is now rotationally symmetric, the Seidel aberration coefficients can be used to describe the third-order aberrations (see Born and Wolf, 1975, pp. 211-218). Therefore, if we define

$$\rho^2 = x^2 + y^2, \tag{3.72}$$

$$\sigma^2 = x_0^2 + y_0^2, \tag{3.73}$$

and

$$\rho\sigma\cos\theta = x_0 x + y_0 y, \tag{3.74}$$

then the final expression for the coded image is given by

$$\Phi_d(\rho,\sigma,\theta) = \frac{2\pi}{\lambda}\left\{\sum_{i=0}^{\infty}\frac{(\frac{1}{2})!}{i!(\frac{1}{2}-i)!}\cdot\frac{\rho^{2i}}{z_r^{2i-1}} + \frac{\mu}{2(a-R)}\left[\frac{\rho^2}{m^2} - 2\frac{\rho\sigma\cos\theta}{m} + \sigma^2\right]\right.$$

$$\sum_{j=0}^{\infty}(-1)^j(j+1)\frac{R^j}{(a-R)^j}\left(\sum_{k=1}^{\infty}\frac{(2k-3)!!}{(2k)!!}\frac{\rho^{2k}}{m^{2k}R^{2k}}\right)^j$$

$$+\frac{\mu}{z_1}\left[\frac{\rho\sigma\cos\theta}{m} + \sigma^2\right]\sum_{j=0}^{\infty}\frac{R^j}{(a-R)^j}\left(\sum_{k=1}^{\infty}\frac{(2k-3)!!}{(2k)!!}\frac{\rho^{2k}}{m^{2k}R^{2k}}\right)^j$$

$$\left.+\frac{\mu(a-R)}{2z_1^2}\sigma^2\right\}. \tag{3.75}$$

The first-, second-, and third-order terms of this expansion are, respectively,

$$\Phi^1 = \frac{2\pi}{\lambda}\left\{\rho^2\left[\frac{1}{2z_r} + \frac{\mu}{2m^2(a-R)}\right] - \rho\sigma\cos\theta\left[\frac{\mu}{m(a-R)} - \frac{\mu}{mz_1}\right]\right.$$

$$\left. + \sigma^2\left[\frac{\mu}{2(a-R)} + \frac{\mu}{z_1} + \frac{\mu(a-R)}{2z_1^2}\right]\right\}. \tag{3.76}$$

$$\Phi^2 = 0, \tag{3.77}$$

and

$$\Phi^3 = \frac{2\pi}{\lambda}\left\{\rho^4\left[-\frac{1}{8z_r^3} - \frac{\mu}{2m^4R(a-R)^2}\right] + \rho^3\sigma\cos\theta\left[\frac{\mu}{m^3R(a-R)^2} + \frac{\mu}{2m^3z_1R(a-R)}\right]\right.$$

$$\left. + \rho^2\sigma^2\left[-\frac{\mu}{2m^2R(a-R)^2} + \frac{\mu}{2m^2z_1R(a-R)}\right]\right\}. \tag{3.78}$$

The first-order terms again give the Gaussian imaging characteristics, with the same results as before:

$$z_g = \frac{z_r}{1 + \dfrac{\mu z_r}{m^2(a-R)}}, \tag{3.79}$$

$$a_g = -x_0\frac{\mu z_g z_2}{mz_1(a-R)}, \tag{3.80}$$

$$b_g = -y_0\frac{\mu z_g z_2}{mz_1(a-R)}, \tag{3.81}$$

where

$$m_s = -m\frac{\mu z_2 z_r}{z_1\left(\mu z_r + m^2(a-R)\right)}. \tag{3.82}$$

From Eq. (3.78), the Seidel aberration coefficients are seen to be

$$W_{040} = -\frac{\mu}{m^2(a-R)}\left[\frac{1}{2m^2R(a-R)} - \frac{3}{8z_r^2} - \frac{3\mu}{8m^2z_r(a-R)} - \frac{\mu^2}{8m^4(a-R)^2}\right]\rho_{max}^4, \tag{3.83}$$

$$W_{131} = \frac{\mu}{m^2(a-R)}\left[\frac{2z_1+(a-R)}{2mz_1R(a-R)} - \frac{m^2(a-R)}{2\mu z_r^3} - \frac{3}{2z_r^2} - \frac{3\mu}{2m^2z_r(a-R)} - \frac{\mu^2}{2m^4(a-R)^2}\right]\rho_{max}^3, \tag{3.84}$$

$$W_{222} = \frac{\mu}{m^2(a-R)}\left[\frac{m^2(a-R)}{2\mu z_r^3} + \frac{3}{2z_r^2} + \frac{3\mu}{2m^2z_r(a-R)} + \frac{\mu^2}{2m^4(a-R)^2}\right]\rho_{max}^2, \tag{3.85}$$

$$W_{220} = \frac{\mu}{m^2(a-R)}\left[\frac{z_2}{4z_1R(a-R)} + \frac{m^2(a-R)}{4\mu z_r^3} + \frac{3}{4z_r^2} + \frac{3\mu}{4m^2z_r(a-R)} + \frac{\mu^2}{4m^4(a-R)^2}\right]\rho_{max}^2, \tag{3.86}$$

$$W_{311} = -W_{222}/\rho_{max}, \tag{3.87}$$

with the total aberration function being

$$W = \sum^{(3)} W_{abc}\rho'^a\sigma^b(\cos\theta)^c. \tag{3.88}$$

In a rotationally-symmetric system, the rms spot size is, to third order, (Shack, 1975).

$$\bar{\varepsilon} = \frac{z_g}{\rho_{max}} \left\{ 2\left[W_{020} + \frac{4}{3} W_{040} + \sigma^2 (W_{220} + \tfrac{1}{2} W_{222}) \right]^2 + \frac{4}{9} W_{040}^2 + \frac{1}{2} \sigma^4 W_{222}^2 + \frac{2}{3} \sigma^2 W_{131}^2 + [W_{111} + \sigma W_{131} + \sigma^3 W_{311}]^2 \right\}^{\frac{1}{2}}. \quad (3.89)$$

Once again, we see that the ratio of the rms spot size to the diffraction-limited spot size can be written as

$$\frac{\bar{\varepsilon}}{d} = \frac{1}{0.61\lambda} W(\sigma). \quad (3.90)$$

As in the case of the cylindrical coded image surface, we will investigate the use of the rms spot size as a means of measuring image quality and present examples of point images in Chapter 5.

The Physical Situation: Imaging with an X-ray Image Intensifier

The electron-beam imaging inside an x-ray image intensifier tube is performed in such a way as to produce the optimum image for an object irradiated by a source point of x-rays located one or two meters from the intensifier screen, depending on the particular intensifier. For nuclear medicine imaging, this means that the optimum imagery would be obtained with the patient located one or two meters from the tube. Therefore, the analysis of the aberrations introduced by the curved input screen may be regarded as being the same as that of the spherical surface (insofar as the input screen may be approximated as a sphere), but with the introduction of a processing function which relates the

x-y projection of the image on the surface to the projection which is the actual intensifier output. It is necessary, then, to find the relationship between a point on the x-y projection of the "fringe" pattern and the corresponding point located by projecting the sphere onto a plane via a focus located a distance D' from the screen.

The situation is shown in Fig. 3.7. The x-y projection coordinate is denoted by r (since the system is rotationally symmetric, the radial measure is sufficient), and the output scale of the intensifier is proportional to r'. The desired processing function is therefore

$$r' = r \cdot g(r). \tag{3.91}$$

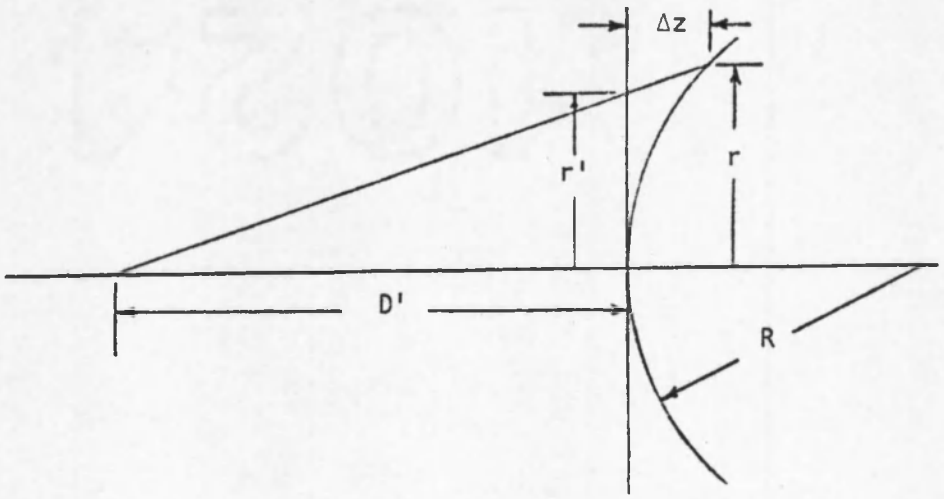

Fig. 3.7. Coordinate Transformation in an X-ray Image Intensifier Tube.

From the diagram,

$$r'(1 + \Delta z/D') = r, \tag{3.92}$$

and

$$\Delta z = R - (R^2 - r^2)^{\frac{1}{2}}. \tag{3.93}$$

Therefore,

$$r' = r \frac{D'}{D' + R - \sqrt{R^2-r^2}}, \tag{3.94}$$

and the processing function is given by

$$g(r) = \frac{D'}{D' + R - \sqrt{R^2-r^2}}. \tag{3.95}$$

It should be noted that an image intensifier which has been adjusted to image as explained above will exhibit no spherical aberration in FZP imaging of an object point located a distance D' from the intensifier, and even for distances of approximately D', the spherical aberration will be considerably smaller than that which would result from simply taking the x-y projection of the coded image. A distorted zone plate would not be needed, then, if the object were located at that particular distance from the screen. Unfortunately, the collection efficiency of the gamma rays will fall off considerably as the object moves away from the screen, and the intensifier tube may no longer be a very efficient way to perform the imaging.

CHAPTER 4

DISTORTION OF THE FRESNEL ZONE PLATE TO CORRECT FOR SPHERICAL ABERRATION

General Theory

In order to eliminate all of the aberrations introduced by the nonplanar coded image surface, it is necessary to either process the reconstructing wavefront or predistort the coded aperture. Since describing the first alternative is beyond the scope of this thesis, we will consider changing the zone plate in some way to reduce or eliminate some or all of the aberrations.

To eliminate all of the aberrations, it would be necessary to use a coded aperture $f'(x,y)$ such that

$$f'\left(\frac{z_1}{z(x,y)}\left[x-x_0\left(1-\frac{z(x,y)}{z_1}\right)\right],\ \frac{z_1}{z(x,y)}\left[y-y_0\left(1-\frac{z(x,y)}{z_1}\right)\right]\right)$$

$$= k\left\{\frac{1}{2z_g}\left[(x-a)^2+(y-b)^2\right]-\frac{1}{8z_g^{\,3}}\left[(x-a)^2+(y-b)^2\right]^2+\cdots\right\}, \tag{4.1}$$

where k is the wave number of the reconstructing wave, a and b are linearly related to x_0 and y_0, respectively, and z_g is the image focal distance. This is probably an impossible condition to meet in all cases for all object points. However, if only one particular

aberration is large enough to be bothersome, then it may be possible to correct for that particular aberration.

In the two systems examined in this thesis, the main image-deforming aberration encountered is spherical, or a spherical-type, aberration. Here, we will examine a means of distorting a FZP to eliminate spherical aberration.

Let the wavefront produced in the exit pupil by the coded image of an axial point source be given by

$$\Phi(x,y) = k\rho^2/2z_g + b'\rho^4 + \cdots , \tag{4.2}$$

where $\rho^2 = x^2+y^2$. If this were produced by a FZP imaged onto a planar surface, then b' would be zero. This means that when the coded image surface is nonplanar, we would like to distort the FZP coded aperture to the form

$$x^2 + y^2 + b(x,y) = c_1^2 n, \tag{4.3}$$

such that the coded image of a particular object point will be a FZP. For an axial object point and a nonplanar surface, the coded image will be

$$\rho^2 \frac{z_1^2}{c_1^2 z^2} + b \frac{z_1^2}{c_1^2 z^2} = n, \tag{4.4}$$

where

$$z = (a-R) + h_1(x,y), \tag{4.5}$$

describes the nonplanar surface.

To generalize the results from the previous chapter, we see that an undistorted FZP will produce a wavefront described by

$$\Phi(x,y) = \rho^2 \frac{z_1^2}{2c_1^2 z^2} = \frac{k}{2z_g} \rho^2 + b'\rho^4. \qquad (4.6)$$

To correct for the spherical aberration, then, we need to find the form of b(x,y) in Eq. (4.3) which will cause b' in Eq. (4.6) to go to zero.

If we use the distorted zone plate in place of the regular FZP, then we see that the x-y projection of the coded image will be given by

$$\rho^2 \frac{z_1^2}{2c_1^2 z^2} + b \frac{z_1^2}{2c_1^2 z^2} = \frac{k}{2z_g^2} + b'\rho^4 + b \frac{z_1^2}{2c_1^2 z^2}. \qquad (4.7)$$

If we then account for the reduction in size of the coded image, and the wavelength of the reconstructing wave, then we see that

$$b = \frac{2c_1^2 z^2 m^4}{z_1^2 \lambda} b'\rho^4, \qquad (4.8)$$

will cause the spherical aberration in the reconstructing wavefront to go to zero, where b' in Eq. (4.8) is the spherical aberration coefficient for the wavefront produced when the regular FZP is used. From Eq. (4.5), we see that

$$z^{-2} = (a-R)^{-2} + h_2(x,y). \qquad (4.9)$$

Obviously, $h_2(x,y)$ will not affect the spherical aberration, so that the final form of the distorted zone plate is given by

$$b(x,y) = - \frac{2c_1^2 m^4 (a-R)^2}{z_1^2 \lambda} b'\rho^4, \qquad (4.10)$$

where b' is the spherical aberration coefficient which results from using a regular FZP.

Aberrations Due to Imaging a Distorted FZP onto a Cylindrical Surface

As shown in Chapter 3, the spherical aberration coefficient W_{400000} is due to both the cylindrical surface and the reconstructing beam. The spherical aberration introduced by the cylindrical surface is

$$W_{cyl} = \rho^4\left(\frac{\mu}{m^2(a-R)}\right)\left[\frac{6R+(a-R)}{24m^2R^2(a-R)}\right]. \tag{4.11}$$

We will use this expression for b' in Eq. (4.10), with the result that the distorted zone plate is described by

$$x^2 + y^2 - \frac{6R+(a-R)}{12R^2(a-R)}\,(x^2+y^2)^2 = c_1{}^2n. \tag{4.12}$$

If a complete analysis of the imaging properties is performed, as with the regular FZP in Chapter 3, then we find that the distortion in the zone plate will introduce additional aberration terms in the reconstructing wavefront, described by

$$\Delta\phi = -\frac{2\pi z_1{}^2}{2z^2c_1{}^2}\left[\left(\frac{x}{m} - x_0\left(1 - \frac{z}{z_1}\right)\right)^2 + \left(\frac{y}{m} - y_0\left(1 - \frac{z}{z_1}\right)\right)^2\right]^2\left[\frac{6R+(a-R)}{12R^2(a-R)}\right], \tag{4.13}$$

with

$$z = a - R\sqrt{1 - \frac{x^2}{R^2}}\,. \tag{4.14}$$

As in the previous section, it is necessary only to let z = (a-R) for the calculation of the third-order aberrations; therefore,

$$\Delta\phi = -\frac{2\pi}{\lambda}\cdot\frac{\mu}{a-R}\left[\frac{6R+(a-R)}{24R^2(a-R)}\right]\left\{\frac{x^2}{m^2}+2\frac{z_2}{mz_1}x_0x+\frac{z_2^2}{z_1^2}x_0^2+\frac{y^2}{m^2}\right.$$

$$\left.+2\frac{z_2}{mz_1}y_0y+\frac{z_2^2}{z_1^2}y_0^2\right\}^2. \qquad (4.15)$$

In terms of the aberrations described in Appendix A, Eq. (4.15) becomes

$$\Delta\phi = -\frac{2\pi}{\lambda}\cdot\frac{\mu}{a-R}\left[\frac{6R+(a-R)}{24R^2(a-R)}\right]\left[\frac{\rho^4}{m^4}+\frac{4z_2}{m^3z_1}\rho^3\sigma\cos(\gamma-\phi)+\frac{2z_2^2}{m^2z_1^2}\rho^2\sigma^2\right.$$

$$\left.+\frac{4z_2^2}{m^2z_1^2}\rho^2\sigma^2\cos^2(\gamma-\phi)+\frac{4z_2^3}{mz_1^3}\rho\sigma^3\cos(\gamma-\phi)+\frac{z_2^4}{z_1^4}\sigma^4\right]. \qquad (4.16)$$

Therefore, we see that introducing the distortion into the FZP has done more than eliminate the spherical aberration--it has also added to the other aberrations. The aberration coefficients which have been changed are

$$W_{400000} = \frac{\mu}{m^2(a-R)}\left[\frac{3}{8z_r^2}+\frac{3\mu}{8m^2z_r(a-R)}+\frac{\mu^2}{8m^4(a-R)^2}\right]\rho_{max}^4, \qquad (4.17)$$

$$W_{311000} = -\frac{\mu}{m^2(a-R)}\left[\frac{6R(3z_1-5z_2)-3z(a-R)}{24mz_1R^2(a-R)}+\frac{m^2(a-R)}{2\mu z_r^3}+\frac{3}{2z_r^2}\right.$$

$$\left.+\frac{3\mu}{2m^2z_r(a-R)}+\frac{\mu^2}{2m^4(a-R)^2}\right]\rho_{max}^3, \qquad (4.18)$$

$$W_{220000} = \frac{\mu}{m^2(a-R)}\left[\frac{3z_1z_2R+z_2^2(6R+(a-R))}{12z_1^2R^2(a-R)} + \frac{m^2(a-R)}{4\mu z_r^3} + \frac{3}{4z_r^2} + \frac{3\mu}{4m^2z_r(a-R)} + \frac{\mu^2}{4m^4(a-R)^2}\right]\rho_{max}^2, \quad (4.19)$$

$$W_{222000} = \frac{\mu}{m^2(a-R)}\left[\frac{z_2^2(6R+(a-R))}{6z_1^2R^2(a-R)} + \frac{m^2(a-R)}{2\mu z_r^3} + \frac{3}{2z_r^2} + \frac{3\mu}{2m^2z_r(a-R)} + \frac{\mu^2}{2m^4(a-R)^2}\right]\rho_{max}^2, \quad (4.20)$$

$$W_{131000} = \frac{\mu}{m^2(a-R)}\left[\frac{z_2^3m(6R+(a-R))}{6z_1^3R^2(a-R)} + \frac{m^2(a-R)}{2\mu z_r^3} - \frac{3}{2z_r^2} - \frac{3\mu}{2m^2z_r(a-R)} - \frac{\mu^2}{2m^4(a-R)^2}\right]\rho_{max}. \quad (4.21)$$

We should note that the distortion described in this section is not the only type of distortion which will eliminate the spherical aberration. In Appendix B, a geometrical method of distorting the zone plate is described that will remove the spherical aberration term. The difference between the two types of distortion is that the distortion described in this chapter will produce a zone plate that is still rotationally symmetric and will not produce a coded image that is a FZP (even though the coded image will have no primary spherical aberration), whereas the distortion described in Appendix B will produce a coded image which is a FZP. Both types of distorted zone plates are examined experimentally in Chapter 5.

Aberrations Due to Imaging a Distorted FZP onto a Spherical Surface

As shown in Chapter 3, the most bothersome aberration encountered in imaging a FZP coded aperture onto a spherical surface is primary spherical aberration. In this section, a distorted zone plate is used instead of the regular zone plate, and the contributions of the zone plate to the wavefront aberrations are calculated.

From Eq. (4.10), we see that the distorted zone plate is described by

$$x^2 + y^2 + \frac{1}{R(a-R)}\,(x^2+y^2)^2 = c_1^2 n. \tag{4.22}$$

As in the previous section, an analysis similar to that of Chapter 3 will show that the spherical aberration is not the only third-order aberration affected by the distortion. An equation analogous to Eq. (4.16) can be derived, namely

$$\Delta\phi(x,y) = \frac{2\pi}{\lambda_0}\cdot\frac{1}{2R(a-R)^2}\left\{\rho^4+4\,\frac{z_2}{z_1}\,\rho^3\sigma\,\cos\theta+2\,\frac{z_2^2}{z_1^2}\,\rho^2\sigma^2+4\,\frac{z_2^2}{z_1^2}\,\rho^2\sigma^2\,\cos^2\theta + 4\,\frac{z_2^3}{z_1^3}\,\rho\sigma^3\,\cos\theta+\frac{z_2^4}{z_1^4}\,\sigma^4\right\}. \tag{4.23}$$

Therefore, the new aberration coefficients are given by

$$W_{040} = \frac{\mu}{m^2(a-R)}\left[\frac{3}{8z_r^2}+\frac{3\mu}{8m^4z_r(a-R)^2}+\frac{\mu^2}{8m^4(a-R)^2}\right]\rho_{max}^4, \tag{4.24}$$

$$W_{131} = \frac{\mu}{m^2(a-R)}\left[\frac{5z_1+3z_2}{2mz_1R(a-R)}-\frac{m^2(a-R)}{2\mu z_r^3}-\frac{3}{2z_r^2}-\frac{3\mu}{2m^2z_r(a-R)} - \frac{\mu^2}{2m^4(a-R)^2}\right]\rho_{max}^3, \tag{4.25}$$

$$W_{222} = \frac{\mu}{m^2(a-R)}\left[\frac{2z_2^2}{z_1^2R(a-R)} + \frac{m^2(a-R)}{2\mu z_r^3} + \frac{3}{2z_r^2} + \frac{3\mu}{2m^2z_r(a-R)} + \frac{\mu^2}{2m^4(a-R)^2}\right]\rho_{max}^2, \tag{4.26}$$

$$W_{220} = \frac{\mu}{m^2(a-R)}\left[\frac{z_1z_2+4z_2^2}{4z_1^2R(a-R)} + \frac{m^2(a-R)}{4\mu z_r^3} + \frac{3}{2z_r^2} + \frac{3\mu}{2m^2z_r(a-R)} + \frac{\mu^2}{2m^4(a-R)^2}\right]\rho_{max}^2, \tag{4.27}$$

$$W_{311} = \frac{\mu}{m^2(a-R)}\left[\frac{2z_2^2m}{z_1^3R(a-R)} - \frac{m^2(a-R)}{2\mu z_r^3} - \frac{3}{2z_r^2} - \frac{3\mu}{2m^2z_r(a-R)} - \frac{\mu^2}{2m^4(a-R)^2}\right]\rho_{max}. \tag{4.28}$$

Again, Chapter 5 will include a comparison of the imagery obtained using the regular and distorted FZP's.

CHAPTER 5

EXPERIMENTAL RESULTS

In order to verify the theoretical work that comprises Chapters 3 and 4 of this thesis, computer calculations were used to quantitatively predict the appearance of reconstructed images of single-point and four-point objects, and then experiments were performed to qualitatively verify the computer predictions. The computer calculations involved the following criteria for evaluating the imagery:

1. Geometrical spot diagrams;
2. The ratio of the geometric rms spot size to the diffraction-limited spot size;
3. The energy distribution as a function of radius; and
4. For a spherical coded image surface, predictions of the reconstructed images of axial objects, accounting for both diffraction and aberrations.

The experimental work supports the spot diagram calculations and the reconstructed image predictions. An optical simulation of a gamma-ray coded imaging system was used to obtain the experimental results. In place of the gamma-ray source, a light box with an appropriate object mask was used. The zone plates used are shown in Figs. 5.1, 5.2, and 5.3. Figure 5.1 shows the regular FZP which was used with both the cylindrical and spherical coded image surfaces. In the

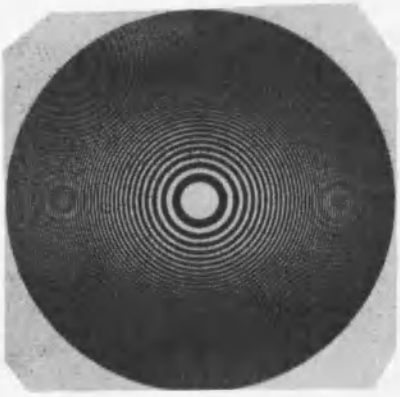

Fig. 5.1. Regular FZP.

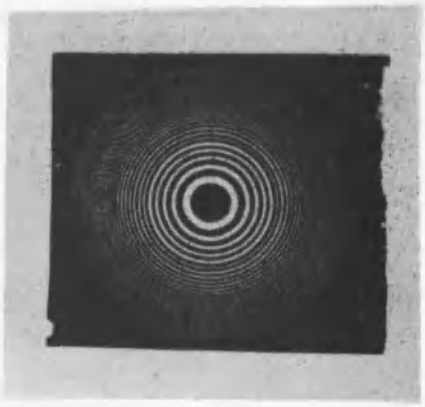

Fig. 5.2. Distorted FZP#1.

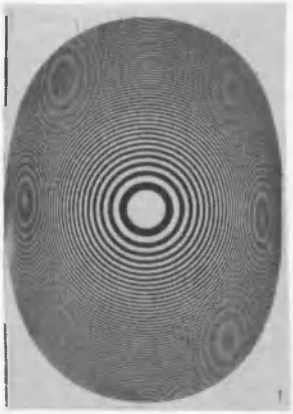

Fig. 5.3. Distorted FZP#2.

experiments, the zone plate was apertured down so that only 32 clear zones were used. Figure 5.2 shows the zone plate which was distorted by the scheme described in Chapter 4. It was also used with both imaging surfaces. When using this zone plate with the cylindrical surface, it was necessary to adjust z_1 and (a-R) slightly in order to satisfy simultaneously Eqs. (4.12) and (4.22), but this minor adjustment would not have affected the results substantially. Figure 5.3 shows the distorted zone plate which was made by the method described in Appendix B. This zone plate was used only for the cylindrical surface. The object distributions used consisted of single pinholes and arrays of four pinholes with the pinholes separated by roughly 2 mm. Both types of objects were placed on-axis and at several off-axis points.

Cylindrical Coded Image Surface

The aberration coefficients for a system using a cylindrical coded image surface are given by Eqs. (3.47) through (3.58) when the regular FZP is used, and by Eqs. (4.17) through (4.21) when the distorted zone plate is used. In the experimental work, the physical parameters had the following values:

Zone plate:	$c_1 = 0.25$ cm
	number of zones = 32
Imaging system:	$z_1 = 5$ cm
	a-R = 10 cm
	R = 12.5 cm

Reconstructing system: $m = 0.04$

$\lambda = 632.8$ nm

$z_r = 50$ cm.

Therefore, the aberration coefficients for the system using the regular FZP, and for the system using the distorted zone plate are given by the values shown in Table 5.1. For the zone plate shown in Fig. 5.3, aberration coefficients were not calculated, but the experimental results which follow will show that such a zone plate is actually superior to either of the other two zone plates.

For the first part of the evaluation, the ratio of the geometric rms spot size to the diffraction-limited spot size was examined. The expression for the rms spot size, as shown in Appendix A, is given by

$$\bar{\varepsilon} = \frac{z_g}{\rho_{max}} W(\sigma,\gamma), \tag{5.1}$$

where $W(\sigma,\gamma)$ is given by the square root of the right-hand side of Eq. (A.20). The expression for $W(\sigma,\gamma)$ is actually quite long and cumbersome. It should be noted, though, that the first four squared expressions locate relative minima in the rms spot size through focal shifts and transverse shifts. The surface containing a minimum can be found by minimizing the sum of the first and fourth expressions, and the image point which gives the minimum rms spot size for a given object point can be found by minimizing the sum of the second and third expressions. Here, we will not be concerned with finding the minimum

Table 5.1. Aberration Coefficients, Cylindrical Surface.

Aberration	Regular FZP	Distorted FZP
W_{400000}	-0.0001464	0.0000037
W_{400010}	0.0001469	0.0001469
W_{400020}	-0.0000173	-0.0000173
W_{311000}	-0.0000159	0.0001310
W_{311010}	0.0000043	0.0000043
W_{310100}	0.0000173	0.0000173
W_{310110}	-0.0000173	-0.0000173
W_{220000}	0.0000443	0.0000627
W_{220010}	-0.0000081	-0.0000081
W_{222000}	0.0000363	0.0000286
W_{131000}	-0.0002264	-0.0002172

spot size, but will use the value of the spot size in the Gaussian image plane as a figure for comparison with the diffraction-limited spot size.

The diffraction-limited spot size is given by

$$d = 0.61\lambda \frac{z_g}{\rho_{max}}, \tag{5.2}$$

and the ratio of the rms spot size to the diffraction-limited spot size is given by

$$\frac{\overline{\varepsilon}}{d} = \frac{1}{0.61\lambda} W(\sigma,\gamma). \tag{5.3}$$

A plot of this ratio as a function of field position is shown in Fig. 5.4 for both the regular and distorted zone plates. In both cases, it is seen that there is little variation in $\overline{\varepsilon}/d$ across the field. This is due to the fact that, in both cases, spherical-type aberrations, in other words, field-independent aberrations, are the dominant aberrations everywhere in the image field. A slight improvement can be realized by using the distorted zone plate, but such a small improvement would probably not justify the correction.

The geometric point spread function can be found in a strict sense by calculating the ray intersection density in the image plane of rays which are normal to the wavefront in the exit pupil. The transverse ray aberrations are related to the wavefront aberrations by

$$\varepsilon_x = -\frac{z_g}{\rho_{max}} \frac{\partial W}{\partial x}, \tag{5.4}$$

and

$$\varepsilon_y = -\frac{z_g}{\rho_{max}} \frac{\partial W}{\partial y}, \tag{5.5}$$

where ε_x and ε_y are the deviations of the ray in the x and y directions from the line joining the center of the exit pupil and the center of the Gaussian reference sphere. Therefore, from Welford (1974, p. 94), the ray intersection density is proportional to

$$I \propto \begin{vmatrix} \frac{\partial^2 W}{\partial x^2} & \frac{\partial^2 W}{\partial x \partial y} \\ \frac{\partial^2 W}{\partial x \partial y} & \frac{\partial^2 W}{\partial y^2} \end{vmatrix}^{-1}. \tag{5.6}$$

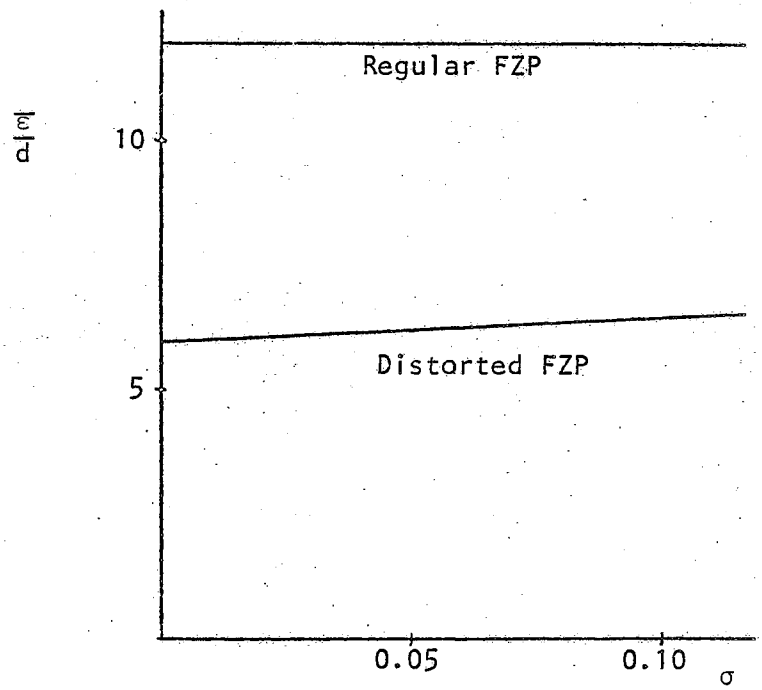

Fig. 5.4. $\frac{\bar{\varepsilon}}{d}$ vs. Field, Cylindrical Coded Image Surface.

However, this becomes infinite on all caustics, so the point spread functions which will be shown were not calculated by using this formula. We can divide the pupil into a set of discrete points, let the ray passing through each point represent a certain amount of energy, and find the number of rays impinging on a small area in the image plane. Since the energy which would be detected is proportional to the number of rays detected, a map of the number of rays intersecting the image plane in each small area would then give a reasonable estimate of the geometrical point spread function. The point spread functions shown in Figs. 5.5 through 5.10 were generated by this method. In these spot diagrams, "A" represents areas where the number of rays is between I_{max} and $I_{max}/2$, where I_{max} is the maximum number of rays impinging on an incremental area, and "B," "C," "D," and "E" each represent successively lower octaves. These figures are to be compared to the experimental results shown in Figs. 5.11 and 5.12. Figure 5.11 shows the image of an axial object point when the regular FZP is used (compare to Fig. 5.5), and Fig. 5.12 shows the image of an axial object point when the distorted zone plate is used (compare to Fig. 5.6). Apparently, the object point used was not exactly centered when the coded image was taken for Fig. 5.12, because the image shows a bit of asymmetry similar to that of Fig. 5.8. Nevertheless, as the $\bar{\epsilon}/d$ ratios would indicate, the use of this type of distorted zone plate will not substantially improve the imagery.

Another use of the geometric point spread function is in calculating the amount of energy contained within a given radius, or,

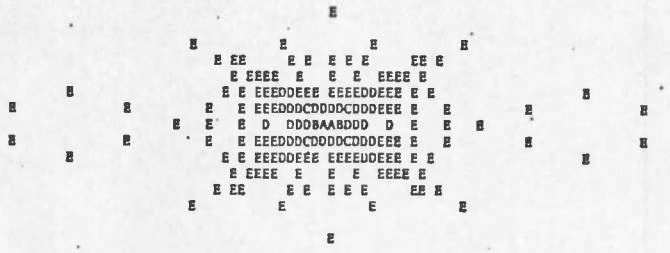

Fig. 5.5. Spot Diagram, Axial Object Point, Regular FZP on Cylindrical Surface, Maximum Count--73.

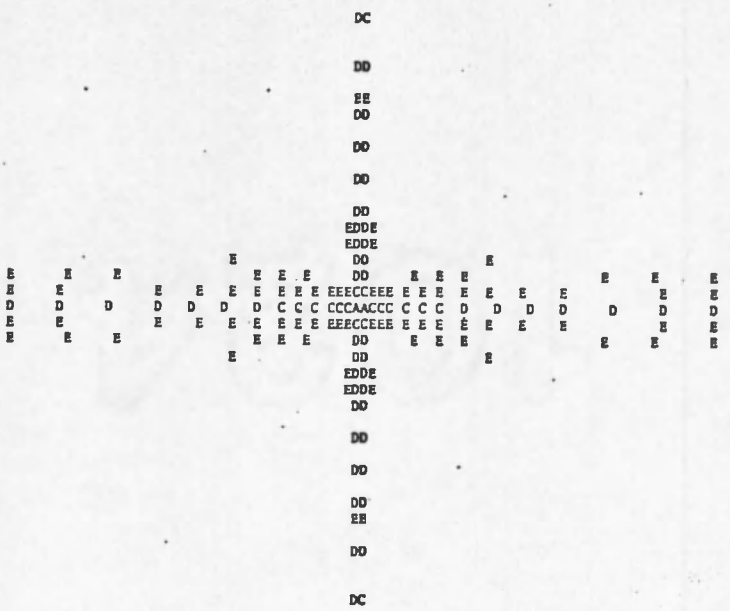

Fig. 5.6. Spot Diagram, Axial Object Point, Distorted FZP #1 on Cylindrical Surface, Maximum Count--64.

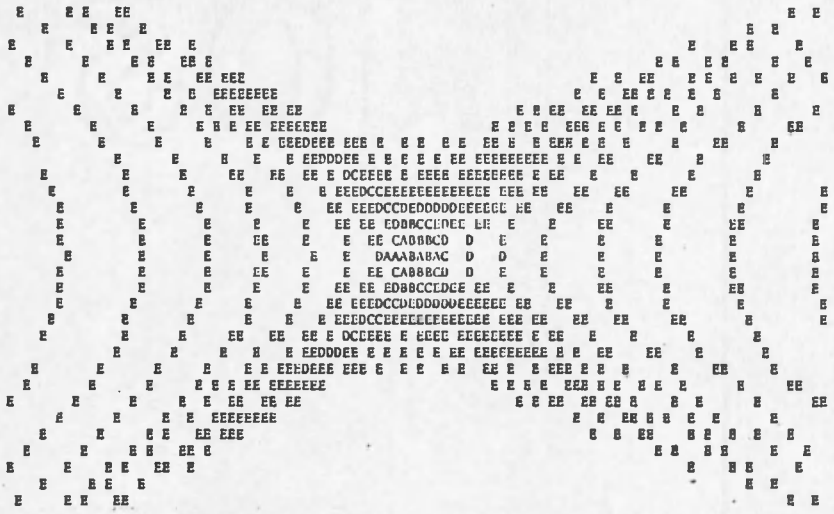

Fig. 5.7. Spot Diagram, Object at x_0 = 1.0 cm, y_0 = 0 cm, Regular FZP on Cylindrical Surface, Maximum Count--51.

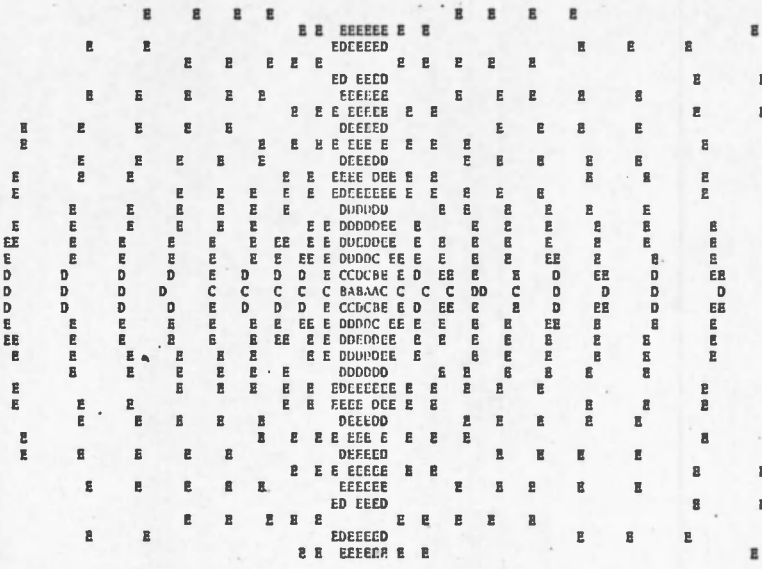

Fig. 5.8. Spot Diagram, Object at x_0 = 1.0 cm, y_0 = 0 cm, Distorted FZP #1 on Cylindrical Surface, Maximum Count--59.

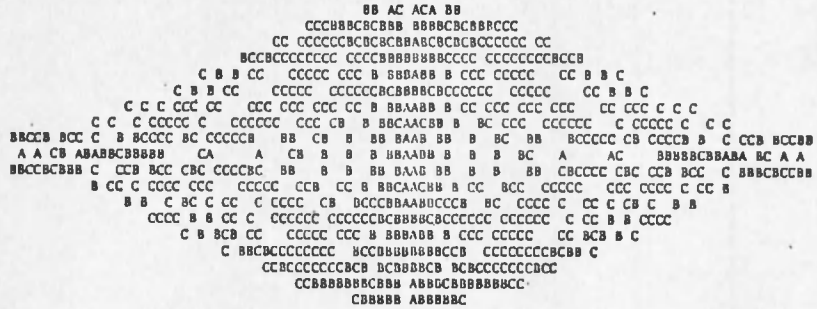

Fig. 5.9. Spot Diagram, Object at x_0 = 0 cm, y_0 = 1.0 cm, Regular FZP on Cylindrical Surface, Maximum Count--10.

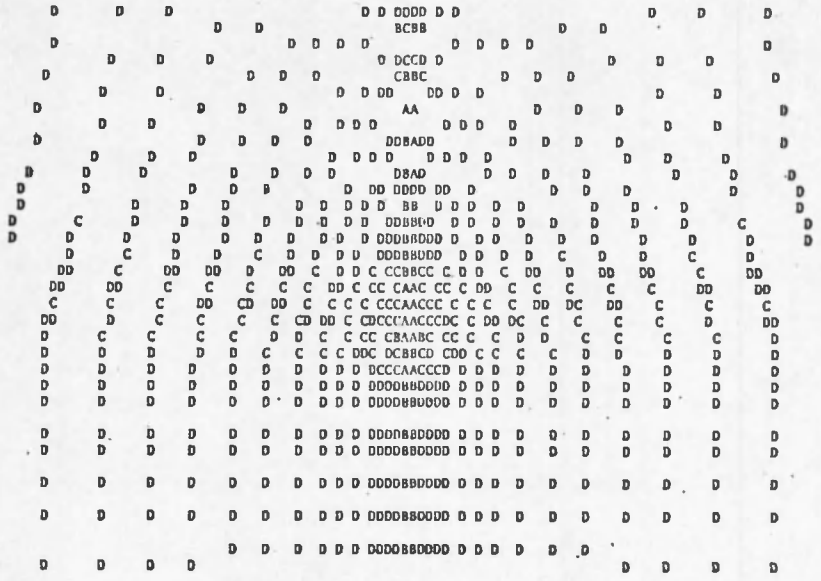

Fig. 5.10. Spot Diagram, Object at x_0 = 0 cm, y_0 = 1.0 cm, Distorted FZP #1 on Cylindrical Surface, Maximum Count--17.

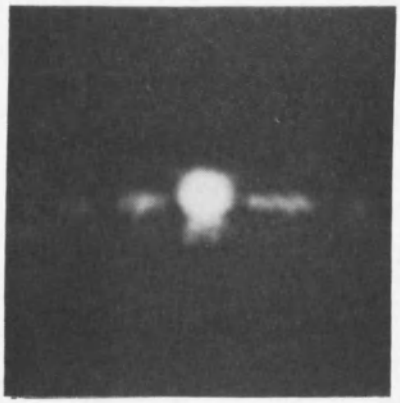

Fig. 5.11. Axial Object Point, Regular FZP on Cylindrical Surface.

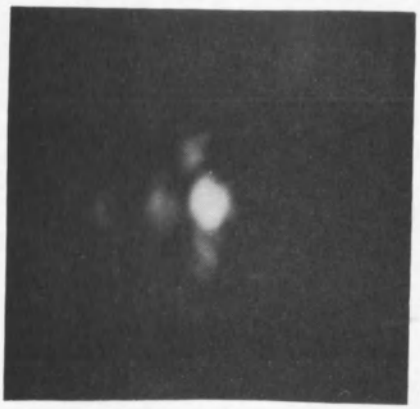

Fig. 5.12. Axial Object Point, Distorted FZP #1 on Cylindrical Surface.

conversely, in calculating the radius within which a given percentage of the total energy is contained. For the system being considered here, the graph in Fig. 5.13 compares this criterion for the regular FZP and the distorted zone plate, with the distorted zone plate showing a slightly higher concentration of energy, as would be expected.

The experimental results shown in Figs. 5.14 through 5.23 show clearly the kind of improvement that can be realized by using the proper type of distorted zone plate. As shown above, the distorted zone plate described in Chapter 4 does not do a very good job of improving the imagery. The reason for this is that the distortion described there will only correct for the type of third-order spherical aberration which is characteristic of a rotationally-symmetric wavefront. Obviously, the aberration coefficients W_{400010} and W_{400020} pertain to wavefront aberrations which are not rotationally symmetric, in other words, to wavefronts that show an optical path difference which depends upon the azimuthal angle in the pupil. As shown in Table 5.1, these nonrotationally-symmetric spherical aberrations are quite large compared to the aberration which is corrected by the distortion, W_{400000}. Therefore, the influence of these aberrations will be large in both cases.

The distorted zone plate described in Appendix B, on the other hand, shows superior imagery in all of the experimental results shown. This is because the zone plate was designed to correct all of the spherical aberration terms, not just the rotationally-symmetric spherical aberration terms. When comparing the results for this zone

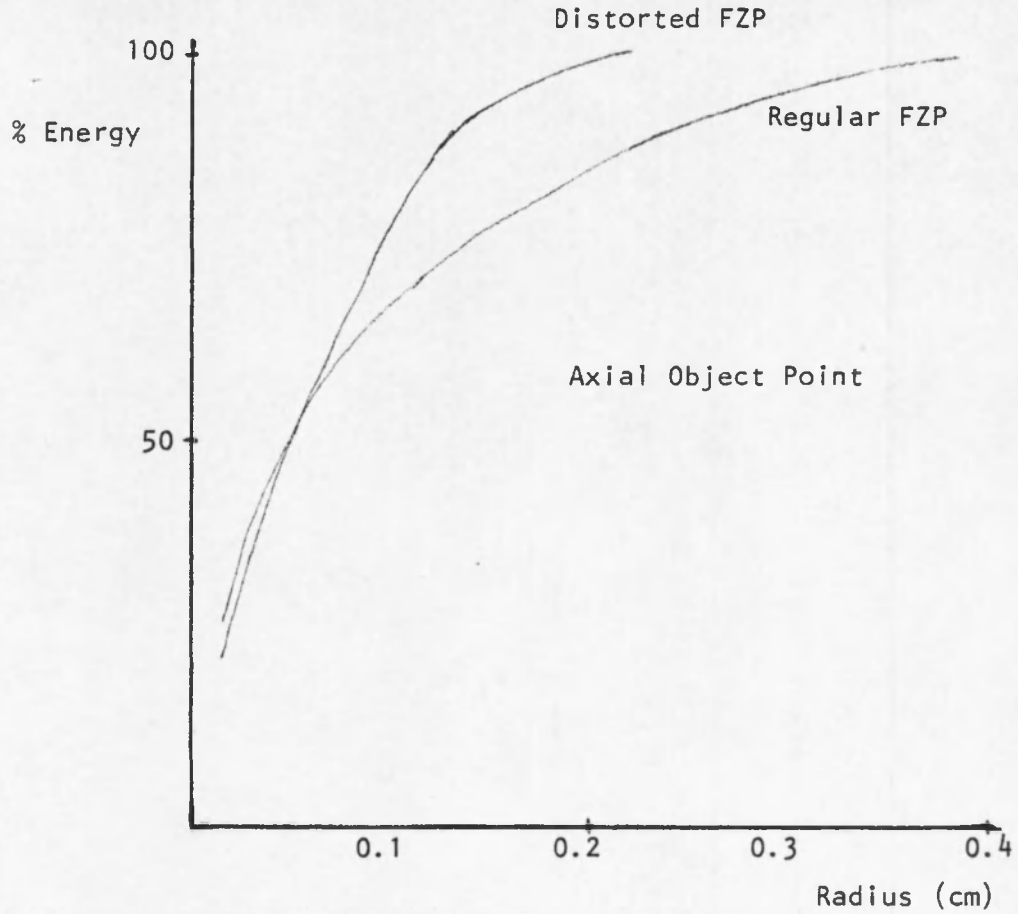

Fig. 5.13. Encircled Energy Cylindrical Coded Image Surface.

Fig. 5.14. Axial Object Point, Distorted FZP #2 on Cylindrical Surface.

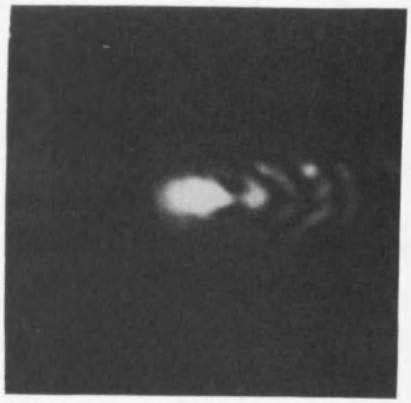

Fig. 5.15. Object Point at x_0 = 1.0 cm, y_0 = 0 cm, Distorted FZP #2 on Cylindrical Surface.

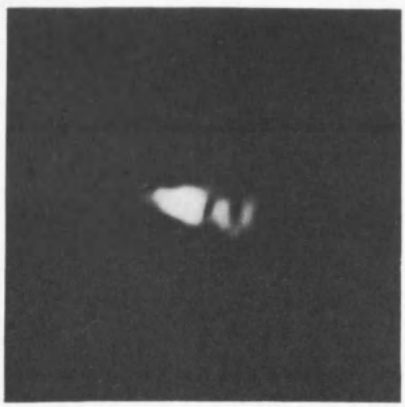

Fig. 5.16. Object Point at x_0 = 0 cm, y_0 = 1.0 cm, Distorted FZP #2 on Cylindrical Surface.

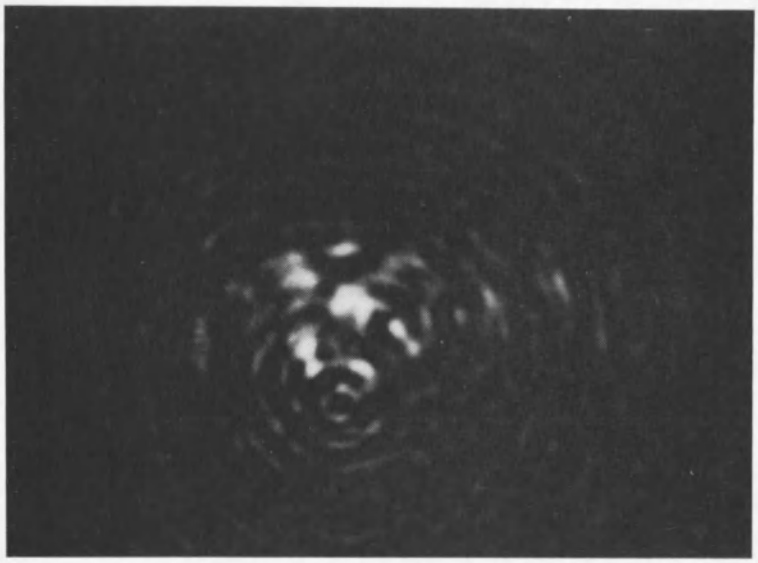

Fig. 5.17. Four-point Axial Object, Regular FZP on Cylindrical Surface.

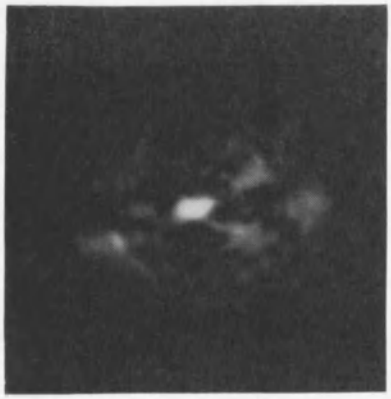

Fig. 5.18. Four-point Axial Object, Distorted FZP #1 on Cylindrical Surface.

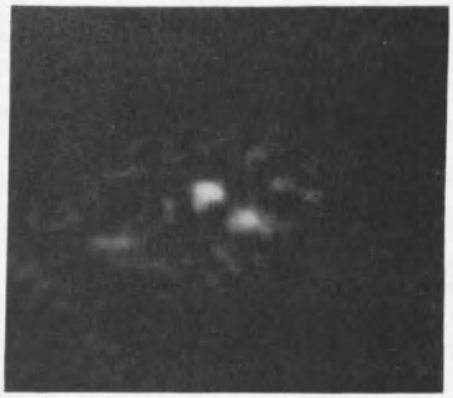

Fig. 5.19. Four-point Object at x_0 = 1.0 cm, y_0 = 0 cm, Distorted FZP #1 on Cylindrical Surface.

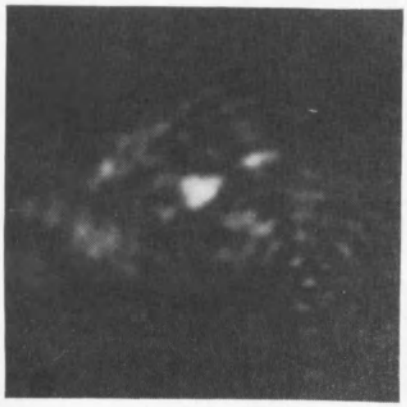

Fig. 5.20. Four-point Object at x_0 = 0 cm, y_0 = 1.0 cm, Distorted FZP #1 on Cylindrical Surface.

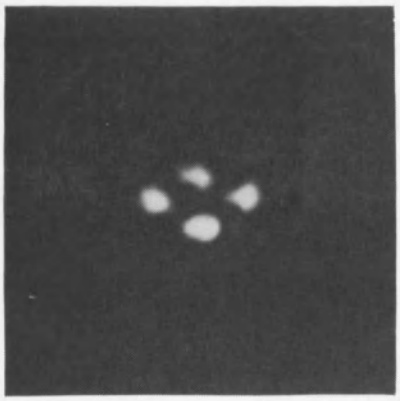

Fig. 5.21. Four-point Axial Object, Distorted FZP #2 on Cylindrical Surface.

Fig. 5.22. Four-point Object at x_0 = 1.0 cm, y_0 = 0 cm, Distorted FZP #2 on Cylindrical Surface.

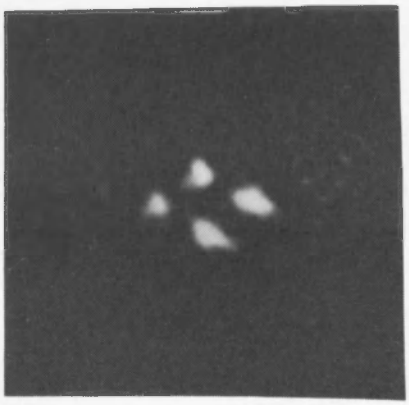

Fig. 5.23. Four-point Object at x_0 = 0 cm, y_0 = 1.0 cm, Distorted FZP #2 on Cylindrical Surface.

plate, though, to the point spread functions generated by the computer for the system using the regular FZP (Figs. 5.5, 5.7, and 5.9), we see that, even though the axial imagery is greatly improved, the point spread function deteriorates much more rapidly for this zone plate as the object moves away from the plane containing the optical axis and the axis of the cylinder than is the case of the regular FZP (the cylinder axis is parallel to the y-axis of the optical system). This means that improved imagery will only be realized for object points near the y-axis of the optical system.

Spherical Coded Image Surface

The aberration coefficients for a system using a spherical coded image surface are given by Eqs. (3.83) through (3.87) when the regular FZP is used, and by Eqs. (4.24) through (4.28) when the distorted zone plate is used. The physical parameters used in the experimental work are identical to those of the system using the cylindrical coded image surface except that the radius of curvature of the coded image surface is 11.7 cm. Again, the system being examined is an optical simulation of the gamma-ray system, with the spherical surface being a ground-glass surface on a plano-convex lens. The aberration coefficients are equal to the values shown in Table 5.2.

In this case, the expression for the rms spot size is given by Eq. (3.89). It is also much easier to determine the focal and transverse shifts needed to go to the point of minimum rms spot size, so we will assume that the imagery is evaluated where the rms spot size is

Table 5.2. Aberration Coefficients, Spherical Surface.

Aberration	Regular FZP	Distorted FZP
W_{040}	-0.0002765	0.0000005
W_{131}	0.0002653	0.0005422
W_{222}	0.0000724	0.0001417
W_{220}	0.0000449	0.0000795
W_{311}	-0.0004527	-0.0004354
W_{400}	-0.0007073	-0.0000313

minimum. Therefore,

$$\frac{\overline{\varepsilon}}{d} = \frac{1}{0.61\lambda}\left[\frac{4}{9}W_{040}^2 + \frac{2}{3}\sigma^2 W_{131}^2 + \frac{1}{2}\sigma^4 W_{222}^2\right]^{\frac{1}{2}}. \qquad (5.7)$$

As before, a plot of $\overline{\varepsilon}/d$ as a function of field position for the system using the regular FZP is flat, as shown in Fig. 5.24, because of the spherical aberration. In this case, the distorted zone plate removes all of the spherical aberration, with the result that the magnitude of $\overline{\varepsilon}/d$ increases linearly with field height, showing the dominance of coma. The magnitude of the ratio is much less in the case of the distorted zone plate, which would seem to indicate much better imagery, but, as will be seen, this is not true. It simply means that more energy will be contained in a smaller area if the distorted zone plate is used.

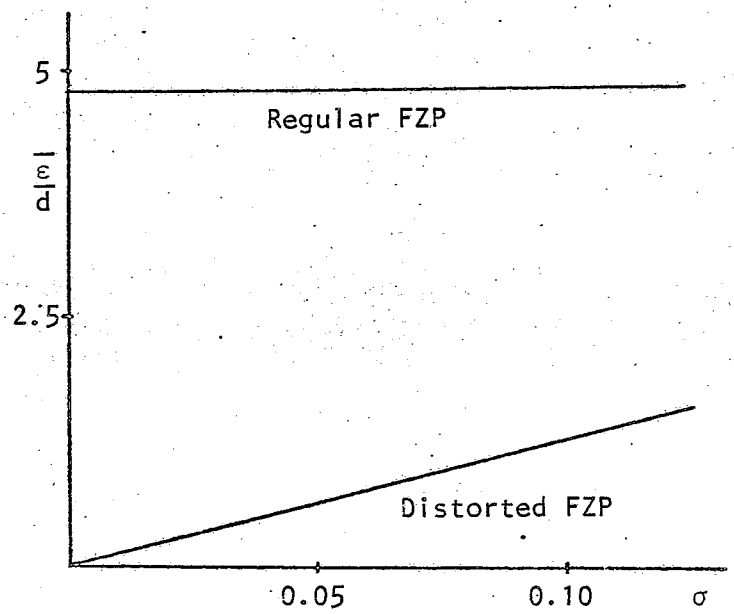

Fig. 5.24. $\frac{\bar{\varepsilon}}{d}$ vs. Field, Spherical Coded Image Surface.

One way to compare the imagery in the two cases is by the aberration tolerances described in Born and Wolf (1975, pp. 468-473). There it is shown that the maximum allowable amounts of aberration which can be present without seriously degrading the imagery are 0.94 waves of spherical aberration or 0.60 waves of coma, when the proper amounts of defocus and transverse shift are included. From Table 5.2, we see that the condition for good imagery is never met when the regular FZP is used, since there will be roughly 4.3 waves of spherical aberration. For the system with the distorted zone plate, the spherical aberration is essentially zero, so that coma, given by σW_{131}, will be the main image-deforming aberration. This will have a value of less than 0.60 waves for all image points such that σ is less than 0.07 cm, or roughly 2 cm in object space. This means that the system will show good imagery for all objects within about 2 cm of the optical axis (in fact, for a two-point object, the imagery will be diffraction-limited for all objects within 2 cm of the optical axis).

Figures 5.25 through 5.30 show the spot diagrams for the system. The diffraction-limited spot size is approximately four times the size of the increment in the spot diagram. Obviously, the energy is spread to a greater extent for the spherically-aberrated wave (Figs. 5.25, 5.27, and 5.29) than for the comatically-aberrated wave (Figs. 5.26, 5.28, and 5.30). If a circle with a radius of two cells (i.e., half of the diffraction spot diameter) is drawn around the apparent maximum in Figs. 5.26, 5.28, and 5.30, though, we see that the energy in the cells just outside this small circle has dropped to less than half of the

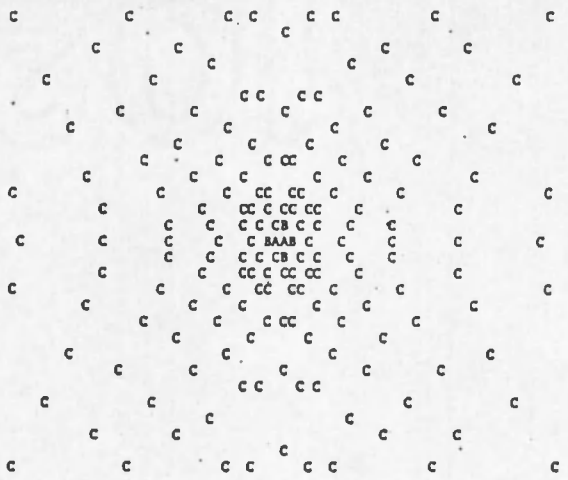

Fig. 5.25. Spot Diagram, Axial Object Point, Regular FZP on Spherical Surface, Maximum Count--13.

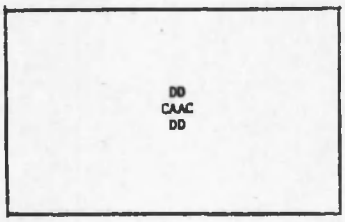

Fig. 5.26. Spot Diagram, Axial Object Point, Distorted FZP on Spherical Surface, Maximum Count--724.

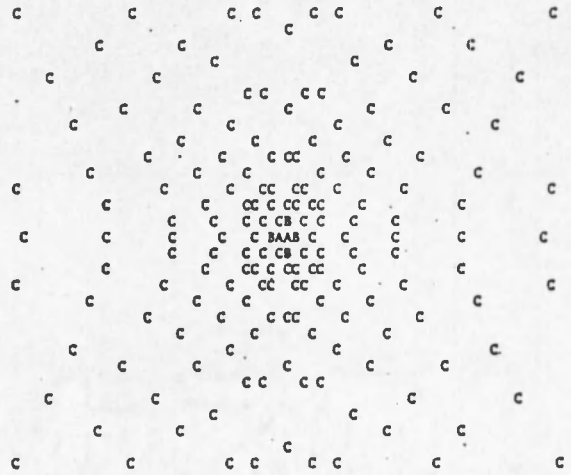

Fig. 5.27. Spot Diagram, x_0 = 0 cm, y_0 = 1.0 cm, Regular FZP on Spherical Surface, Maximum Count--14.

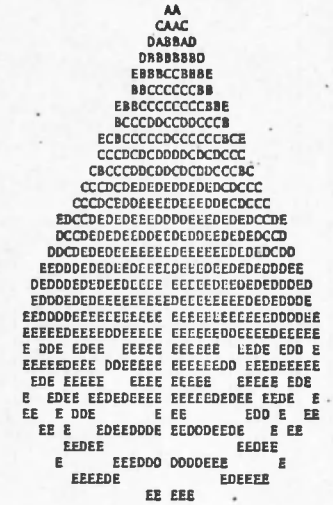

Fig. 5.28. Spot Diagram, x_0 = 0 cm, y_0 = 1.0 cm, Distorted FZP on Spherical Surface, Maximum Count--47.

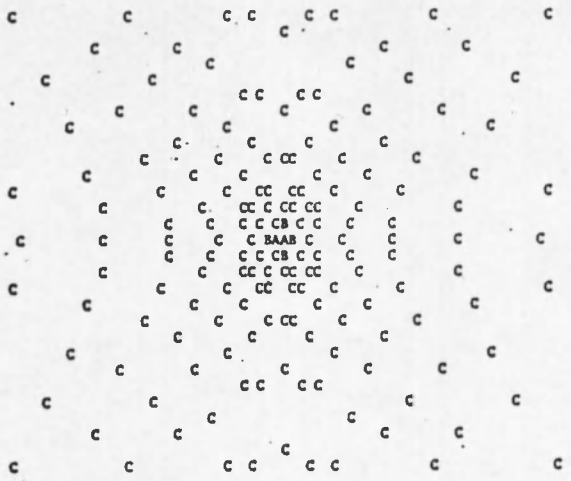

Fig. 5.29. Spot Diagram, x_0 = 0 cm, y_0 = 2.0 cm, Regular FZP on Spherical Surface, Maximum Count--13.

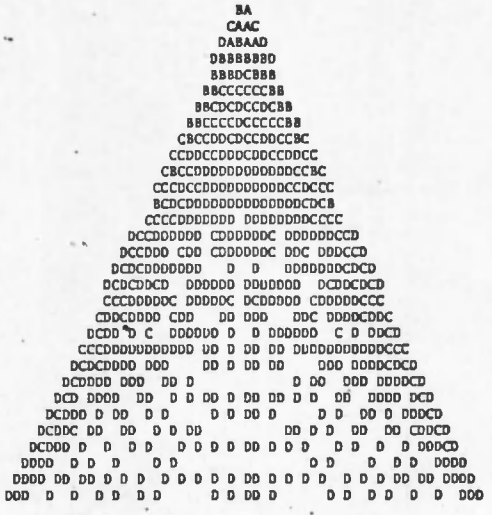

Fig. 5.30. Spot Diagram, x_0 = 0 cm, y_0 = 2.0 cm, Distorted FZP on Spherical Surface, Maximum Count--24.

maximum. This, in turn, means that two points separated by a distance equal to the diameter of the Airy disk are barely resolvable, which supports the tolerance calculations described above.

Figure 5.31 shows the graph of the energy contained within circles of given radii, centered on the Gaussian focus, for point images when the regular and distorted FZP's are used. This shows that the energy is much more concentrated when the distorted FZP is used, even out to large fields. Like the rms spot size, though, this criterion for image quality does not appear to be a good indicator in light of the spot diagrams and the tolerance criteria presented above.

Figures 5.32 and 5.33 show the experimental resuslts obtained by using single-point axial objects with a regular FZP (Fig. 5.32) and a distorted zone plate (Fig. 5.33). The two images appear comparable, except for some messiness in Fig. 5.33 which is due to imperfections in the distorted zone plate (see Fig. 5.2), and a small increase in the central intensity of the image in Fig. 5.33 relative to that of the image in Fig. 5.32 (this is not readily apparent in this pair of photos, but can be observed by taking underexposed pictures of the point images).

Figures 5.34 and 5.35 show the experimental results obtained by using a single-point object placed 0.5 cm from the axis. In Fig. 5.34, we see that, in addition to the spherical aberration, there is also a bit of coma produced by the regular FZP (about 0.077 waves for this field height). In Fig. 5.35, we see the obvious presence of coma

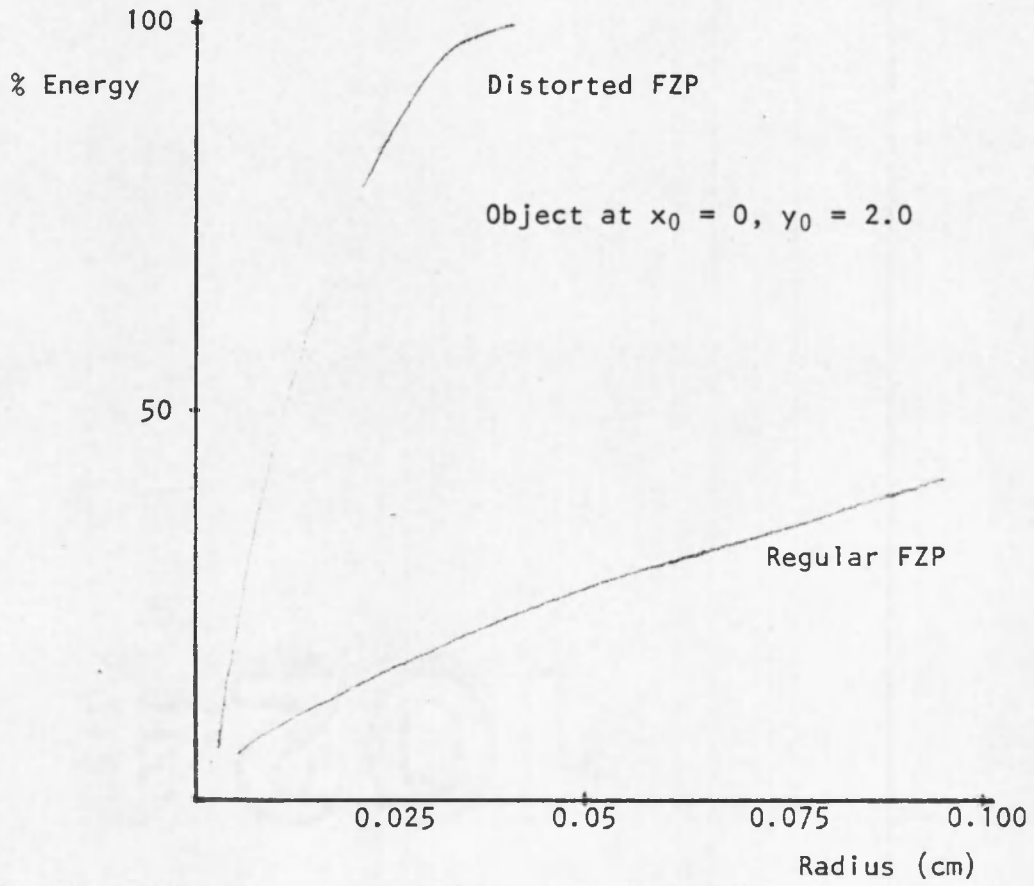

Fig. 5.31. Encircled Radius Spherical Coded Image Surface.

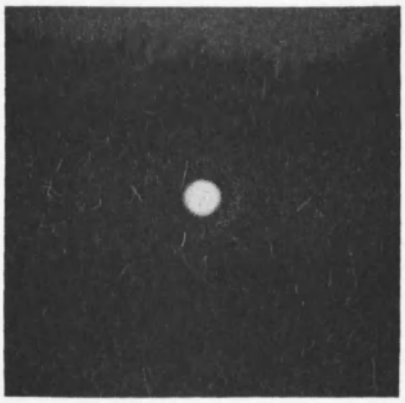

Fig. 5.32. Axial Object Point, Regular FZP on Spherical Surface.

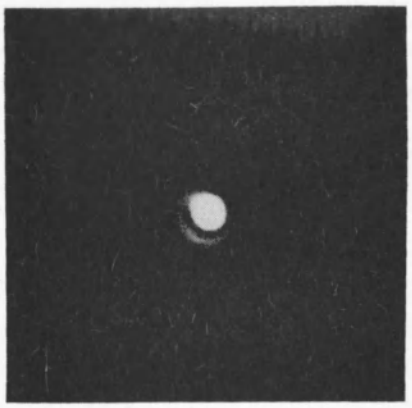

Fig. 5.33. Axial Object Point, Distorted FZP on Spherical Surface.

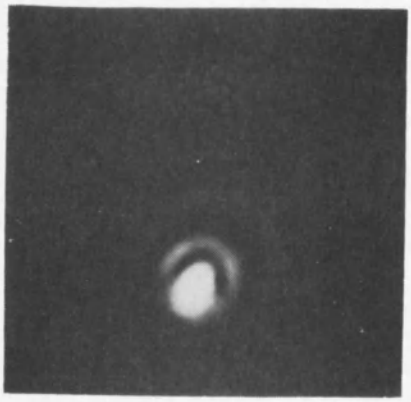

Fig. 5.34. Object Point at x_0 = 0 cm, y_0 = 0.5 cm, Regular FZP on Spherical Surface.

Fig. 5.35. Object Point at x_0 = 0 cm, y_0 = 0.5 cm, Distorted FZP on Spherical Surface.

(approximately 0.15 waves) in the reconstructed image of the point source with the distorted zone plate.

For this system, a coherent point spread function was calculated following Born and Wolf (1975, p. 461) in order to more accurately predict experimental results, and the calculation was used to predict the image of an axial four-point object when using the regular FZP. This prediction is shown in Fig. 5.36. This clearly shows the effect that spherical aberration can have on an image. For a point object, spherical aberration will not affect the diffraction-spot diameter, until large amounts of aberration are present. It will simply cause a decrease in the maximum amplitude in the point spread function. Therefore, a single point will still be imaged as a single point, but more complex objects will not be accurately imaged. This is shown clearly in the figure.

The experimental results, Figs. 5.37 through 5.40, show, first of all, that the computer prediction is at least qualitatively valid, and second, that there is considerable improvement to be gained in imaging objects near the axis by using the distorted zone plate. Unfortunately, the improvement again quickly disappears as the object moves away from the axis. At 0.5 cm, the points are still resolvable, as the tolerance criteria in Born and Wolf (1975, pp. 468-473) would indicate. The image may appear worse than it actually is, though, because the film is a high-contrast film (Polaroid type 107). One thing that we should make note of is that the exposure required to obtain Fig. 5.39 is four times as long as that required for Fig. 5.40.

This demonstrates quite vividly that the distorted zone plate is concentrating more energy nearer to the Gaussian focus.

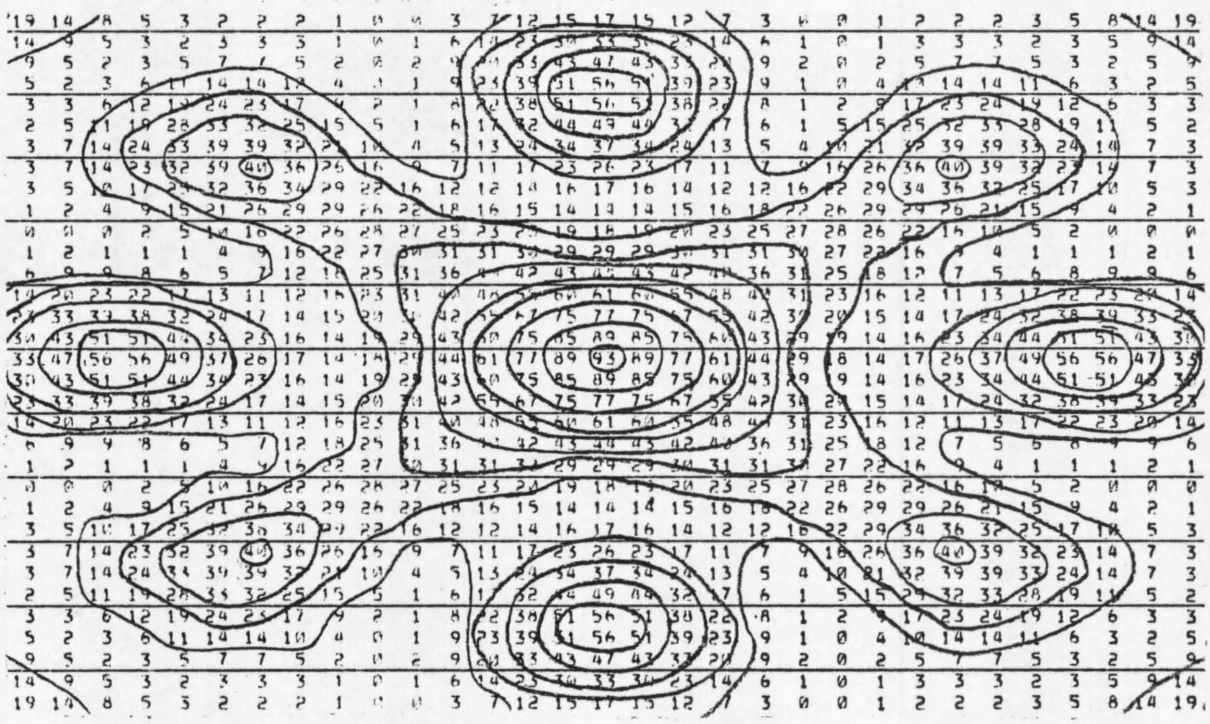

Fig. 5.36. Four-point Axial Object, Predicted Diffraction Image, Regular FZP on Spherical Surface.

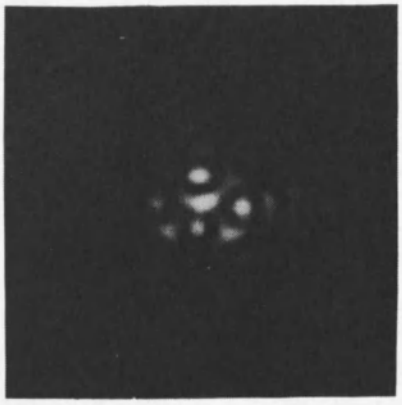

Fig. 3.37. Four-point Axial Object, Regular FZP on Spherical Surface.

Fig. 5.38. Four-point Axial Object, Distorted FZP on Spherical Surface.

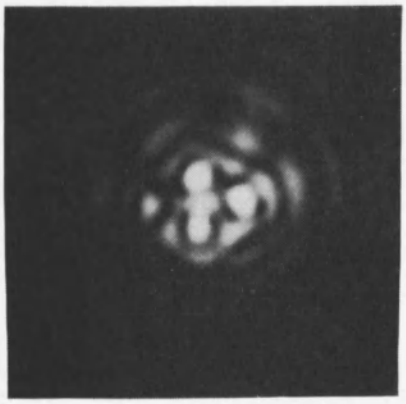

Fig. 5.39. Four-point Object at x_0 = 0 cm, y_0 = 0.5 cm, Regular FZP on Spherical Surface.

Fig. 5.40. Four-point Object at x_0 = 0 cm, y_0 = 0.5 cm, Distorted FZP on Spherical Surface.

CHAPTER 6

CONCLUSION

It has been shown, first of all, that a curved coded image surface can seriously degrade an image in a coded aperture imaging system. The aberrations have been calculated for a system with a cylindrical coded image surface and for a system with a spherical coded image surface. It is seen that, in both cases, spherical aberrations are the dominant image-deforming aberrations which are present in the reconstructed image. A method of eliminating the primary spherical aberration has been examined, and it is concluded that proper distortion of the zone plate will improve the imagery over a small region of the object plane.

One possibility for further investigation would be to perform the aberration correction in the reconstruction step rather than in the encoding step. It would seem that if a spherically-aberrated wave were used as the reconstructing wavefront, then the spherical aberration present in the coded image could be exactly cancelled, without any contributions to the other aberrations.

Also, it is evident that the image quality for systems which have aberrations as large as those encountered here is not accurately described by the rms spot size or by the encircled energy in the reconstructed image. The aberration tolerance criterion seems to work well

for point objects, but it is not clear that it will be accurate when more complex objects are imaged. It would be useful to investigate some other criterion, such as the optical transfer function, as a means of measuring the quality of reconstructed images of more complex objects, and to apply this to the problem discussed in this thesis.

APPENDIX A

ABERRATION COEFFICIENTS FOR A SYSTEM WITH TWO MUTUALLY-ORTHOGONAL SYMMETRY AXES

It is desirable to be able to deal with aberrations in an optical system containing two mutually orthogonal planes of symmetry. An example of such a system is one in which a rotationally-symmetric coded aperture is imaged onto a cylindrically-shaped film plane. When the resulting coded image is inserted into the usual reconstruction system, it transforms the system from a rotationally-symmetric system to a system of two mutually-orthogonal symmetry axes. The general treatment of aberrations in a nonrotationally-symmetric system is treated by Baraket and Houston (1966) in terms of the Hamilton mixed characteristic $W(x_0,y_0;p,q)$, where x_0 and y_0 are the object plane coordinates and p and q are the exit pupil coordinates. They show that, for a system with two mutually-orthogonal planes of symmetry, the aberration function is described by

$$W(x_0,y_0;p,q) = W^{(0)} + W^{(2)} + W^{(4)} + \cdots, \tag{A.1}$$

where $W^{(0)}$ is a constant which can be set equal to zero, and

$$W^{(2)} = B_1p^2 + B_2x_0p + B_3y_0q + B_4q^2 \tag{A.2}$$

$$W^{(4)} = D_1p^4 + D_3p^2q^2 + D_5q^4 + D_6x_0p^3 + D_8x_0pq^2 + D_{11}y_0p^2q + D_{13}y_0q^3 + D_{14}x_0^2p^2 + D_{15}x_0^2q^2 + D_{17}y_0^2q^2 + D_{18}y_0^2p^2$$

$$+ D_{22}x_0y_0pq + D_{23}x_0^3p + D_{26}y_0^3p + D_{28}x_0^2y_0q$$
$$+ D_{30}x_0y_0^2p, \qquad (A.3)$$

where the B and D values can be related to specific geometrical aberration curves. These expressions can be compared directly to the terms of the series expansion in the text to get a spot diagram in the image plane. In this Appendix, I shall develop an expression for the rms spot size of an image obtained using this sort of system.

The coordinate system is shown in Fig. A.1, and it is assumed that the object and image coordinates are linearly related, and that normalized pupil coordinates are used. The wavefront expansion will be described by

$$W(x,y;x_0,y_0) = \sum_{a=0}^{\infty} \sum_b \sum_c \sum_d \sum_e \sum_f W_{abcdef}\rho^{2a}\sigma^{2b}[\rho\sigma\cos(\gamma-\phi)]^c$$
$$\cdot\ [\rho\sigma\cos(\gamma+\phi)]^d[\rho^2\cos 2\phi]^e[\sigma^2\cos 2\gamma]^f. \qquad (A.4)$$

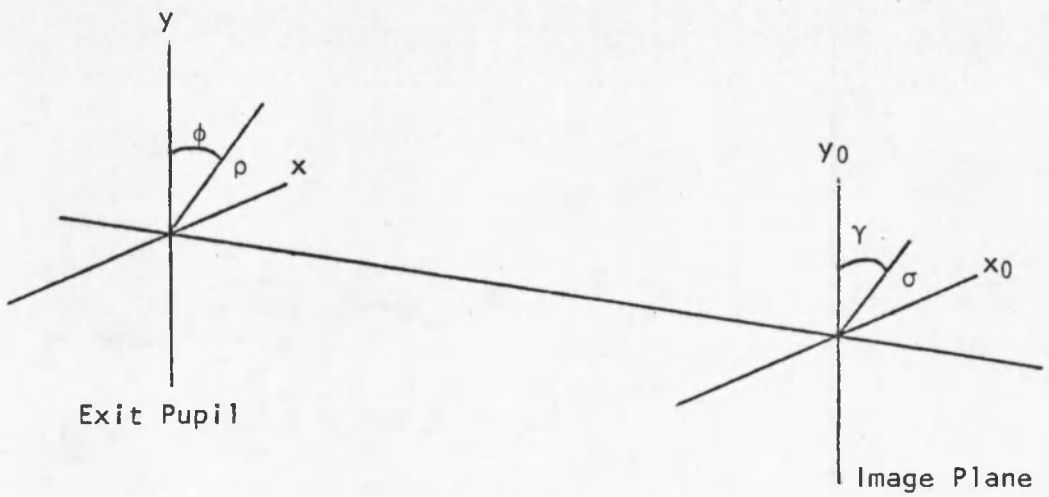

Fig. A.1. System with Two Mutually-orthogonal Symmetry Axes.

This will completely describe the wavefront if it is recognized that a few of the terms must be omitted due to redundancy. That this expansion completely describes the wavefront is seen from the fact that the six "building blocks" of the aberration function are equal to

$$x^2 = \frac{1}{2}(\rho^2 - \rho^2 \cos 2\phi)$$

$$x_0^2 = \frac{1}{2}(\sigma^2 - \sigma^2 \cos 2\gamma)$$

$$y^2 = \frac{1}{2}(\rho^2 + \rho^2 \cos 2\phi)$$

$$y_0^2 = \frac{1}{2}(\sigma^2 + \sigma^2 \cos 2\gamma)$$

$$x_0 x = \frac{1}{2}\left(\rho\sigma \cos(\gamma-\phi) - \rho\sigma \cos(\gamma+\phi)\right)$$

$$y_0 y = \frac{1}{2}\left(\rho\sigma \cos(\gamma-\phi) + \rho\sigma \cos(\gamma+\phi)\right). \qquad (A.5)$$

Letting

$$W_{\alpha cde} = \sum_{b=0}^{\infty} \sum_{f} W_{\alpha\beta cdef} \sigma^{\beta} [\cos 2\gamma]^f, \qquad (A.6)$$

where $\alpha = 2a + 2e + c + d$, and $\beta = 2b + 2f + c + d$, then

$$W = \sum^{(4)} W_{\alpha cde} \rho^{2a} (y \cos\gamma + x \sin\gamma)^c (y \cos\gamma - x \sin\gamma)^d (y^2 - x^2)^e. \qquad (A.7)$$

The rms spot size of a point image formed by a wavefront described by $W(x,y;x_0,y_0)$ is given by

$$\overline{\varepsilon} = R/(nr) \cdot \left(\int \left[\left(\frac{\partial W}{\partial y}\right)^2 + \left(\frac{\partial W}{\partial x}\right)^2 \right] \rho d\rho d\phi \right)^{\frac{1}{2}}, \qquad (A.8)$$

where R is the distance from the pupil to the image plane, r is the radius of the exit pupil, and n is the refractive index of the image space.

Here,

$$\frac{\partial W}{\partial x} = \sum^{(4)} W_{\alpha cde} \rho^{\alpha-1} [\cos(\gamma-\phi)]^{c-1} [\cos(\gamma+\phi)]^{d-1} [\cos 2\phi]^{e-1}$$

$$\cdot \{2(a \cos 2\phi - e) \sin\phi \cos(\gamma-\phi) \cos(\gamma+\phi)$$

$$+ [c \cos(\gamma+\phi) - d \cos(\gamma-\phi)] \sin\gamma \cos 2\phi\}, \quad (A.9)$$

and

$$\frac{\partial W}{\partial y} = \sum^{(4)} W_{\alpha cde} \rho^{\alpha-1} [\cos(\gamma-\phi)]^{c-1} [\cos(\gamma+\phi)]^{d-1} [\cos 2\phi]^{e-1}$$

$$\cdot \{2(a \cos 2\phi + e) \cos\phi \cos(\gamma-\phi) \cos(\gamma+\phi)$$

$$+ [c \cos(\gamma+\phi) + d \cos(\gamma-\phi)] \cos\gamma \cos 2\phi\}, \quad (A.10)$$

where, to third order, the aberration terms $W_{\alpha cde}$ are the 12 terms

$$a_1 = W_{2000}$$

$$a_2 = W_{1100}$$

$$a_3 = W_{1010}$$

$$a_4 = W_{2001}$$

$$a_5 = W_{3100}$$

$$a_6 = W_{3010}$$

$$a_7 = W_{4001}$$

$$a_8 = W_{3101}$$

$$a_9 = W_{3011}$$

$$a_{10} = W_{4000}$$

$$a_{11} = W_{2200}$$

$$a_{12} = W_{4002}. \qquad \text{(A.11)}$$

In terms of the six parameters a, b, c, d, e, and f, these are

$$W_{2000} = W_{200000} + W_{220000} + W_{220001}$$

$$W_{1100} = W_{111000} + W_{131000} + W_{131001}$$

$$W_{1010} = W_{110100} + W_{130100} + W_{130101}$$

$$W_{2001} = W_{200010} + W_{220010} + W_{220011}$$

$$W_{3100} = W_{311000}$$

$$W_{3010} = W_{310100}$$

$$W_{4001} = W_{40010}$$

$$W_{3101} = W_{311010}$$

$$W_{3011} = W_{310110}$$

$$W_{4000} = W_{400000}$$

$$W_{2200} = W_{222000}$$

$$W_{4002} = W_{400020}, \qquad \text{(A.12)}$$

and it has been recognized that $W_{2110} = W_{221100}$ and $W_{2020} = W_{220200}$, which would ordinarily arise in the general expansion of the series, are algebraically equal to combinations of other terms:

$$W_{221100} \rightarrow \rho^2\sigma^2 \cos(\gamma-\phi)\cos(\gamma+\phi) = \rho^2\sigma^2[\tfrac{1}{2}(1+\cos2\phi)+\tfrac{1}{2}(1+\cos2\gamma)-1]$$

$$= \tfrac{1}{2}\rho^2\sigma^2\cos2\phi + \tfrac{1}{2}\rho^2\sigma^2\cos2\gamma$$

$$\therefore\ W_{221100} \rightarrow W_{220010},\ W_{220001} \qquad (A.13)$$

$$W_{220200} \rightarrow \rho^2\sigma^2\cos^2(\gamma+\phi) = \rho^2\sigma^2[\cos^2\gamma\cos^2\phi - 2\cos\gamma\cos\phi\sin\gamma\sin\phi + \sin^2\gamma\sin^2\phi]$$

$$= \tfrac{1}{2}\rho^2\sigma^2[1+\cos2\phi\cos2\phi - \cos^2(\gamma-\phi)]$$

$$\therefore\ W_{220200} \rightarrow W_{220000},\ W_{220011},\ W_{222000}. \qquad (A.14)$$

Squaring the expressions for $\partial W/\partial y$ and $\partial W/\partial x$ is equivalent to multiplying each by a new series, therefore,

$$\left(\frac{\partial W}{\partial x}\right)^2 = \sum_i^{(4)}\sum_j^{(4)} W^i W^j \rho^{\alpha_i+\alpha_j-2}[\cos(\gamma-\phi)]^{c_i+c_j-2}[\cos(\gamma+\phi)]^{d_i+d_j-2}$$

$$\cdot\ [\cos2\phi]^{e_i+e_j-2}\{2(a_i\cos2\phi-e_i)\sin\phi\cos(\gamma-\phi)\cos(\gamma+\phi)$$

$$+ [c_i\cos(\gamma+\phi) - d_i\cos(\gamma-\phi)]\sin\gamma\cos2\phi\}\cdot\{2(a_j\cos2\phi-e_j)$$

$$\cdot\ \sin\phi\cos(\gamma-\phi)\cos(\gamma+\phi) + [c_i\cos(\gamma+\phi) - d_j\cos(\gamma-\phi)]$$

$$\sin\gamma\cos2\phi\}, \qquad (A.15)$$

and there is a similar expression for $(\partial W/\partial y)^2$.

Since the integral in the equation for the rms spot size is to be taken over the exit pupil, it can be rewritten as

$$\frac{\bar{\varepsilon}^2}{\left(\frac{R}{nr}\right)^2} = \frac{1}{\pi}\int_0^{2\pi} d\phi \int_0^1 \left[\left(\frac{\partial W}{\partial x}\right)^2 + \left(\frac{\partial W}{\partial y}\right)^2\right]\rho' d\rho' \qquad (A.16)$$

where ρ' is the normalized pupil radius, $\rho' = \rho/\rho_{max}$.

When the two squared expressions are added and put into the integral, the equation can be simplified to the form

$$\frac{\bar{\varepsilon}^2}{\left(\frac{R}{nr}\right)^2} = \frac{1}{\pi}\sum^{(8)} W^i W^j \frac{1}{\alpha_i+\alpha_j}\; 4\Big(a_i a_j + e_i a_j + e_j a_i + \tfrac{1}{2}\Big[a_i\left(c_j+d_j\right) + a_j\left(c_i+d_i\right)\Big]\Big) \int_0^{2\pi} [\cos(\gamma-\phi)]^{c_i+c_j}[\cos(\gamma+\phi)]^{d_i+d_j}[\cos 2\phi]^{e_i+e_j} d\phi$$

$$+ 4e_i e_j \int_0^{2\pi} [\cos(\gamma-\phi)]^{c_i+c_j}[\cos(\gamma+\phi)]^{d_i+d_j}[\cos 2\phi]^{e_i+e_j-2} d\phi$$

$$+ 2\left(e_i c_j + e_j c_i\right) \int_0^{2\pi} [\cos(\gamma-\phi)]^{c_i+c_j-1}[\cos(\gamma+\phi)]^{d_i+d_j+1}[\cos 2\phi]^{e_i+e_j-1} d\phi$$

$$+ 2\left(e_i d_j + e_j d_i\right) \int_0^{2\pi} [\cos(\gamma-\phi)]^{c_i+c_j+1}[\cos(\gamma+\phi)]^{d_i+d_j-1}[\cos 2\phi]^{e_i+e_j-1} d\phi$$

$$+ c_i c_j \int_0^{2\pi} [\cos(\gamma-\phi)]^{c_i+c_j-2}[\cos(\gamma+\phi)]^{d_i+d_j}[\cos 2\phi]^{e_i+e_j} d\phi$$

$$+ d_i d_j \int_0^{2\pi} [\cos(\gamma-\phi)]^{c_i+c_j} [\cos(\gamma+\phi)]^{d_i+d_j-2} [\cos 2\phi]^{e_i+e_j} d\phi$$

$$+ \cos 2\gamma \left(c_i d_j + c_j d_i\right) \int_0^{2\pi} [\cos(\gamma-\phi)]^{c_i+c_j-1} [\cos(\gamma+\phi)]^{d_i+d_j-1} [\cos 2\phi]^{e_i+e_j} d\phi \; . \qquad (A.17)$$

Therefore,

$$\frac{\bar{\varepsilon}^2}{\left(\frac{R}{nr}\right)^2} = 2a_1^2 + (16/3)a_1a_{10} + 2a_1a_{11} + (8/3)a_1a_{12} + a_2^2$$

$$+ (2\cos 2\gamma)a_2a_3 + 2a_2a_5 + (2\cos 2\gamma)a_2a_6 + (\cos 2\gamma)a_2a_8$$

$$+ a_2a_9 + a_3^2 + (2\cos 2\gamma)a_3a_5 + 2a_3a_6 + a_3a_8 + (\cos 2\gamma)a_3a_9$$

$$+ 2a_4^2 + 2a_4a_7 + (2\cos 2\gamma)a_4a_{11} + (5/3)a_5^2 + (10\cos 2\gamma/3)a_5a_6$$

$$+ (5\cos 2\gamma/3)a_5a_8 + (5/3)a_5a_9 + (5/3)a_6^2 + (5/3)a_6a_8$$

$$+ (5\cos 2\gamma/3)a_6a_9 + (5/2)a_7^2 + (2\cos 2\gamma)a_7a_{11} + (4/3)a_8^2$$

$$+ (7\cos 2\gamma/3)a_8a_9 + (7/6)a_9^2 + 4a_{10}^2 + (8/3)a_{10}a_{11}$$

$$+ 4a_{10}a_{12} + a_{11}^2 + (4/3)a_{11}a_{12} + 2a_{12}^2. \qquad (A.18)$$

This can be expressed as the sum of perfect squares:

$$\frac{\bar{\varepsilon}^2}{\left(\frac{R}{nr}\right)^2} = A_1(a_1+A_2a_{10}+A_3a_{11}+A_4a_{12})^2 + B_1(a_2 + \cdots)^2 + \cdots, \qquad (A.19)$$

where A_1, A_2, etc., are determined from the coefficients above.

Therefore,

$$\frac{\overline{\varepsilon}^2}{\left(\frac{R}{nr}\right)^2} = 2\Big[(W_{200000} + \sigma^2 W_{220000} + \sigma^2 \cos 2\gamma W_{220001}) + \frac{4}{3} W_{400000} + \frac{1}{2}\sigma^2 W_{220000} + \frac{2}{3} W_{400020}\Big]^2$$

$$+ [(\sigma W_{111000} + \sigma^3 W_{131000} + \sigma^3 \cos 2\gamma W_{131001}) + \cos 2\gamma(\sigma W_{110100} + \sigma^3 W_{130100} + \sigma^3 \cos 2\gamma W_{130101}) + \sigma W_{311000} + \sigma \cos 2\gamma W_{310100} + \tfrac{1}{2}\sigma \cos 2\gamma W_{311010} + \tfrac{1}{2}\sigma W_{310110}]^2$$

$$+ (1-\cos^2 2\gamma)[(\sigma W_{110100} + \sigma^3 W_{130100} + \sigma^3 \cos 2\gamma W_{130101}) + \sigma W_{310100} + \tfrac{1}{2}\sigma W_{311010}]^2$$

$$+ 2[(W_{200010} + \sigma^2 W_{220010} + \sigma^2 \cos 2\gamma W_{220011}) + \tfrac{1}{2} W_{400010} + \tfrac{1}{2}\sigma^2 \cos 2\gamma W_{222000}]^2$$

$$+ \frac{2}{3}(1-\cos^2 2\gamma)[\sigma W_{310100} + \tfrac{1}{2}\sigma W_{311010}]^2$$

$$+ 2[W_{400010} + \tfrac{1}{4}\sigma^2 \cos 2\gamma W_{222000}]^2$$

$$+ \frac{3}{4}[\sigma W_{311010} + \sigma \cos 2\gamma W_{310110}]^2$$

$$+ \frac{3}{4}(1-\cos^2 2\gamma)[\sigma W_{310110}]^2$$

$$+ \frac{4}{9}[W_{400000} + \tfrac{1}{2} W_{400020}]^2$$

$$+ \left(\frac{1}{2} - \frac{5}{8}\cos^2 2\gamma\right)[\sigma^2 W_{222000}]^2 + [W_{400020}]^2. \qquad \text{(A.20)}$$

This will give the geometric rms spot size anywhere in the image field. The first four terms locate the image surface and the centroid to which the spot size will be referred. For example, if the first and second brackets are set equal to zero, then the remaining terms determine the rms spot size with respect to one point in the image space, whereas if the first and third brackets are set equal to zero, then the remaining terms determine the rms spot size with respect to another, generally different, point.

APPENDIX B

DISTORTION OF ZONE PLATE FOR IMAGING ONTO A CYLINDRICAL SURFACE

As shown in Chapter 4, it is desirable to distort the zone plate in such a way as to eliminate the third-order spherical aberration. For the case of a spherical-imaging surface, this can be done by simply computing new radii for the zones and making a new circular zone plate. With a cylindrical imaging surface, the new zone plate will not be rotationally symmetric, and even though the coordinates of the required zones can be calculated, using these calculations is physically rather difficult. For the work done in this thesis, a corrected zone plate was used which was produced by bending the original FZP to the proper radius and casting a shadow, using a point source, onto a flat piece of film. Here I will use a simple geometric proof to show that a zone plate made in this way will produce no spherical aberration in the final image.

If a particular zone plate can be imaged onto a surface by an axial object point with the resulting coded image being, to at least third order, a Fresnel Zone Plate, then the reconstructed image will exhibit no third-order spherical aberration. The problem in this case is to develop a zone plate which will produce the FZP on a piece of film fastened to a cylindrical form. In Fig. B.1, assume that the curved film surface is S_1 and that the original FZP is placed on

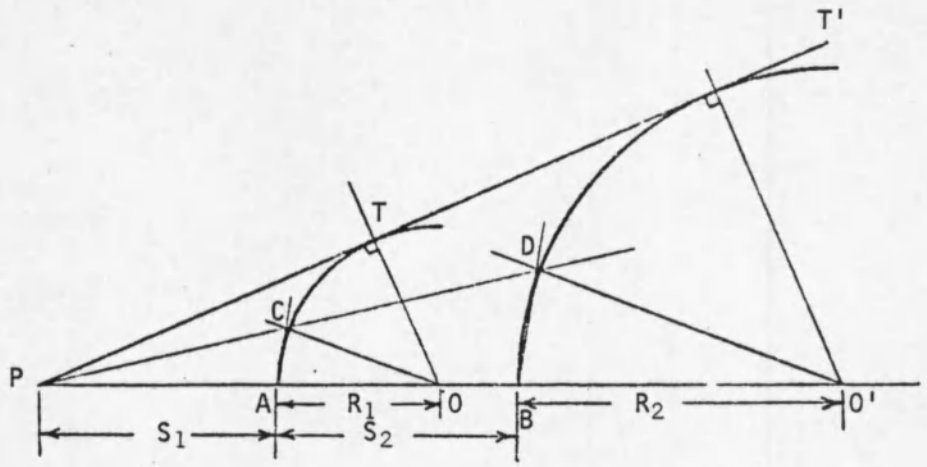

Fig. B.1. Geometrical Distortion of Zone Plate.

surface S_2. As the following proof shows, the circumferential distances on S_1 will be in the same ratio as the circumferential distances on S_2.

$$\Delta PTO \sim \Delta PT'O'$$

$$\therefore \measuredangle TOA = \measuredangle T'O'B$$

$$\widehat{TA}/\widehat{CA} = \measuredangle TOA/\measuredangle COA$$

$$\widehat{T'B}/\widehat{DB} = \measuredangle T'O'B/\measuredangle DO'B$$

$$\therefore \widehat{TA}/\widehat{CA} = \widehat{T'B}/\widehat{DB}$$

$$\therefore \measuredangle COA = \measuredangle DO'B$$

$$\therefore \Delta COA \sim \Delta DO'B$$

$$\therefore CA/DB = R_1/R_2$$

$$CA \,||\, DB$$

$\therefore$ $\Delta PCA \sim \Delta POB$

$\therefore$ $CA/DB = z_1/(a-R)$.

Therefore, if the arc lengths are to be in the same ratio, then

$R_1/R_2 = z_1/(a-R)$.

REFERENCES

Baraket, R., and A. Houston (1966), Optica Acta 13, 1.

Barrett, H. H. (1972), J. Nucl. Med. 13, 382.

Barrett, H. H., and F. A. Horrigan (1973), Appl. Opt. 12, 2686.

Barrett, H. H., and G. D. DeMeester (1974), Appl. Opt. 13, 1100.

Born, M., and E. Wolf (1975), Principles of Optics, 5th ed., Pergamon Press, New York.

Dicke, R. H. (1968), Astrophys. J. 153, L101.

Fonroget, J., Y. Belvaux, and S. Lowenthal (1975), Optics Comm. 15, 76.

Golay, M. J. E. (1971), J. Opt. Soc. Am. 61, 272.

Henkelman, R. M., and M. J. Bronskill (1974), J. Opt. Soc. Am. 64, 134.

Joy, M. L. G., and S. Houle (1975), IEEE Trans. Nucl. Med. NS-22, 364.

Mertz, L., and N. D. Young (1961), in Proceedings of the International Conference on Optical Instruments, Chapman and Hall, p. 365.

Shack, R. V. (1975), Class Notes, Optical Sciences 204, The University of Arizona, Tucson, Arizona.

Stigliani, D. J., R. Mittra, and R. G. Semonin (1967), J. Opt. Soc. Am. 57, 610.

Walton, P. W. (1973), J. Nucl. Med. 14, 861.

Welford, W. T. (1974), Aberrations of the Symmetrical Optical System, Academic Press, London.

Young, M. (1972), J. Opt. Soc. Am. 62, 972.